






# PAH Products and Processing by Different Energy Sources

G. A. Cruz-Diaz<sup>1,2</sup> , S. E. Erickson<sup>3</sup>, E. F. da Silveira<sup>4</sup>, A. Ricca<sup>2,5</sup> , A. L. F. de Barros<sup>2,6</sup> , C. A. P. da Costa<sup>4</sup>,  
R. C. Pereira<sup>6</sup>, and A. L. Mattioda<sup>2</sup>

<sup>1</sup> Bay Area Environmental Research Institute, Moffett Field, Mountain View, CA 94035, USA; [gustavo.a.cruzdiaz@nasa.gov](mailto:gustavo.a.cruzdiaz@nasa.gov)

<sup>2</sup> NASA Ames Research Center, Moffett Field, Mountain View, CA 94035, USA

<sup>3</sup> University of Minnesota, Twin Cities, Minneapolis, MN, USA

<sup>4</sup> Departamento de Física, Pontifícia Universidade Católica do Rio de Janeiro (PUC-Rio), Rua Marquês de São Vicente, 225, 22453-900, Rio de Janeiro, Brazil

<sup>5</sup> Carl Sagan Center, SETI Institute, 189 Bernardo Avenue, CA 94043, USA

<sup>6</sup> Departamento de Física, Centro Federal de Educação Tecnológica Celso Suckow da Fonseca (CEFET-RJ), Av. Maracanã, 229, 20271-110, Rio de Janeiro, RJ, Brazil

Received 2018 September 24; revised 2019 May 16; accepted 2019 July 9; published 2019 August 30

## Abstract

Isoviolanthrene (C<sub>34</sub>H<sub>18</sub>), a polycyclic aromatic hydrocarbon (PAH) molecule, was studied via matrix isolation in argon and water at 20 K. Infrared spectroscopy was performed in situ where samples were irradiated using ultraviolet light. Experimental spectra were compared to theoretical spectra for vibrational band assignment, determination of the corresponding A-values, and photoproduct identification. Isoviolanthrene was also deposited as a thin film and irradiated with different energy sources: ultraviolet photons (10.2 eV), soft electrons (1.5 keV), protons (1.5 MeV), and He<sup>+</sup> particles (1.5 MeV), to understand the effects of different energy sources on a PAH. Anions and cations of isoviolanthrene were produced as a result of UV photolysis in an argon matrix. Hydrogen- and oxygen-rich aromatic photoproducts were produced by ultraviolet photons when isoviolanthrene was isolated in a water matrix. The irradiated PAH thin films results were dependent on the energy source. Irradiation with ultraviolet photons yielded a broad underlying feature centered at 9.6 μm, while bombardment with soft electrons gave a broad feature centered at 7.7 μm. In the case of proton bombardment, no broad feature was detected, in contrast with He<sup>+</sup> bombardment that destroyed most of the isoviolanthrene and produced broad features in the C-Hoop and C-H stretching regions. A comparison of astronomical IR emission observations with our experimental results in the mid-infrared range has revealed a similarity between the observed plateaus and the broad features produced by our experiments.

*Key words:* astrochemistry – infrared: ISM – methods: laboratory: molecular – molecular processes – techniques: spectroscopic

## 1. Introduction

Polycyclic aromatic hydrocarbons (PAHs) are ubiquitous in space and contribute to the observed emission bands at 3.3, 6.2, 7.7, 8.6, 11.3, and 12.7 μm (Allamandola et al. 1989; Tielens 2008; Sloan et al. 2014 and references therein). They have been detected in lines of sight of reflection nebulae, photodissociation regions, and the Galactic center. Under these different environments, PAHs experience different types of radiations (e.g., ultraviolet photons, electrons, and cosmic rays) that can potentially process and degrade them.

Stecher (1965) first reported the 2175 Å ultraviolet extinction absorption feature in 1965. Since then, groups from all over the world have dedicated observation time to characterize this feature and identify its carrier (see Savage et al. 1985; Valencic et al. 2004; Halasinski et al. 2005; Fitzpatrick & Massa 2007; Blasberger et al. 2017). Steglich et al. (2010, 2012) studied this problem in the laboratory using a size distribution of PAH molecules. They performed matrix-isolation experiments using neon gas as well as deposition of thin films. They found that large matrix-isolated PAH molecules (>22 carbon atoms) could reproduce the UV absorption feature at 2175 Å. On the other hand, small matrix-isolated PAH molecules (<22 carbon atoms) did not present a good fit for this absorption feature. In the case of thin films (PAH clusters or PAHs on dust grain analogs), they concluded that PAHs with more than 22 carbon atoms have the best fit in width and shape to the interstellar UV bump.

PAH clusters behave similarly to nano-sized carbonaceous particles that exhibit a strong UV absorption (e.g., Rapacioli et al. 2005). They have been suggested as possible emitters contributing to the broad plateaus underlying the active mid-infrared (mid-IR) emission features in the interstellar medium (ISM); see Allamandola et al. (1989).

Micelotta et al. (2011) studied the effects of cosmic-ray ions (H<sup>+</sup>, He<sup>+</sup>, CNO, and Fe–Co–Ni) and electrons on PAHs by calculating the nuclear and electronic interactions for the collisions. Their study found that small PAHs are destroyed faster with He<sup>+</sup> and CNO groups, indicating the high effectiveness of these particles. In the case of electrons, the destruction rate was independent of PAH size. Micelotta et al. (2011) concluded that PAHs in space could be destroyed by thermal ions and electrons taking place in galactic halos, outflows of galaxies, and the intra-cluster medium. However, soft electrons are ineffective in dense clouds due to the low penetration depth. Nevertheless, PAHs protected in dense clouds can still be processed by the penetration of cosmic rays and X-rays into the cloud.

Isoviolanthrene A (IVA, C<sub>34</sub>H<sub>18</sub>, benzo[*rst*]phenanthro[10,1,2-*cde*]pentaphene, CAS No. 4430-29-9) is a PAH molecule that exhibits an elongated open structure, with a dark red color, consisting of nine six-membered rings. IVA was chosen to be the subject of study in the O/OREOS mission (see Bramall et al. 2012; Mattioda et al. 2012; Cook et al. 2014, and Ehrenfreund et al. 2014). It was deposited as a thin film, enclosed in three different astrobiologically relevant

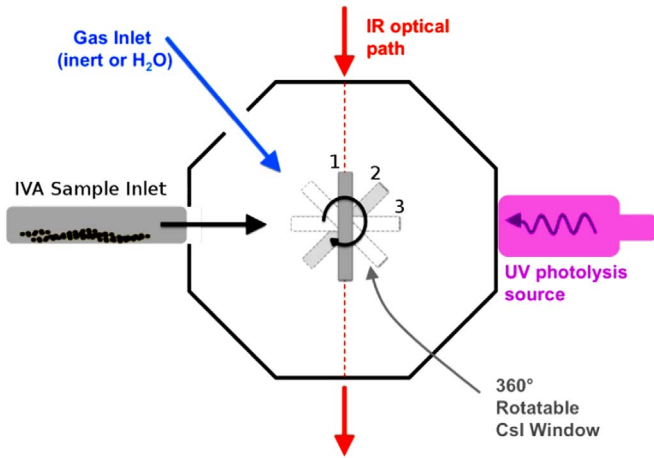


**Figure 1.** Schematic of the high-vacuum setup used in our matrix-isolation experiments. Position 1 is used to irradiate the deposited sample by UV photons and soft electrons. Position 2 is used in the codeposition of Ar/H<sub>2</sub>O and IVA. Position 3 is used for FTIR data collection.

microenvironments, and exposed to direct solar illumination in low Earth orbit. The macroenvironment sample cells were: Inert, 100 kPa of argon; Atmosphere, 1 kPa of CO<sub>2</sub>, 0.001 kPa of O<sub>2</sub> and balanced argon to 100 kPa; and Humid, 100 kPa of argon with 0.8 to 2.3% relative humidity. Mattioda et al. (2012) reported that the three IVA samples (Inert, Atmosphere, and Humid) presented little to no spectral change. However, the Humid microenvironment presented a significant decrease in the intensity of the main IVA absorption feature centered at  $\sim 350$  nm in the UV/Vis region, implying that the material was processed by solar radiation. This decrease in band intensity correlates with the increase in accumulated UV dose. Later, in laboratory experiments, that decrease in the IVA was attributed to the formation of an oxidation product, CO<sub>2</sub>. However, due to the spectral window cutoff of the microenvironment cells, no other photoproduct was confirmed via infrared measurements.

Here we report the irradiation of IVA deposited in an argon (i.e., Inert cell) matrix, in a water matrix (i.e., Humid cell), and as a thin film. The molar absorptivities or optical cross-section (*A*-values) are reported for neutral IVA for which experiments and theory are compared. Ion bands, and their *A*-values, produced by UV irradiation of matrix-isolated IVA are also presented and compared to theoretical values. Differences in the decrease rates for the vibrational bands of IVA thin film by UV photons (Ly $\alpha$ ), soft electrons, and high-energy particles (H<sup>+</sup> and He<sup>+</sup>) are also presented and discussed.

## 2. Experimental Protocol

Samples were deposited on an infrared transparent Csl window cooled to 20 K by direct codeposition inside a high-vacuum chamber ( $1 \times 10^{-8}$  torr); see Figure 1. Argon gas (Ar) was used for matrix-isolation studies (Ar, Matheson Gas Products, ULSI 6N), and in some instances, to separate the cation from the anion bands, the argon gas was doped with NO<sub>2</sub> (Aldrich, 99.5%), an electron acceptor that prevents the formation of anions. For water-matrix-isolation experiments, Milli-Q grade filtered, and deionized water was used. Contaminant gases were removed from the water by three freeze-pump-thaw cycles. IVA was purchased from the PAH Research Institute and had a purity of 99.5%. IVA was deposited as vapor, thermally sublimated from a Pyrex tube

hermetically sealed and directly attached to the vacuum chamber. The sublimation temperature for IVA was  $\approx 380^\circ\text{C}$ . Samples were irradiated with UV photons using a microwave-discharged hydrogen flow lamp that has a robust Ly $\alpha$  and low molecular hydrogen emission, simulating the irradiation experienced by interstellar matter. The UV flux was  $\approx (2 \pm 0.5) \times 10^{14}$  photons  $\text{cm}^{-2} \text{s}^{-1}$ , as determined by actinometry measurements using polyethylene films (Truica-Marasescu & Wertheimer 2005; Alata et al. 2014). UV lamps produce a Ly $\alpha$  emission band followed by the H<sub>2</sub> molecular emission. They have an average output energy of  $\approx 10.2$  eV at the sample position; see Chen et al. (2014) and Cruz-Diaz et al. (2014) for a detailed description of these lamps. Samples were monitored via FTIR from 4000 to 450  $\text{cm}^{-1}$  using a Biorad Excalibur FTS 4000 FTIR spectrometer equipped with a KBr beamsplitter and a liquid N<sub>2</sub>-cooled MCT detector. A low-energy flood electron gun (EFG-8K, Kimball Physics) with an output of 1.5 keV was used in our experiments. The electron flux was calculated using the Richardson–Dushman equation

$$J = \mathcal{A}T^2 e^{-\phi/\kappa T}, \quad (1)$$

where  $J$  is the emission current density in  $\text{A cm}^{-2}$ ,  $\mathcal{A}$  is the Richardson’s constant ( $37 \text{ A cm}^{-2} \text{K}^{-2}$ ),  $T$  is the cathode temperature in K (1860 K),  $\phi$  is the work function of the cathode material in eV (4.1 eV), and  $\kappa$  is the Boltzmann’s constant ( $8.6 \times 10^{-5} \text{ eV K}^{-1}$ ). Considering that  $1 \text{ A} = 6.25 \times 10^{18} \text{ electrons s}^{-1}$ , we calculated an electron flux of  $3 \times 10^{15} \text{ electrons cm}^{-2} \text{s}^{-1}$ .

Three kinds of matrix-isolation experiments were performed, following the method described in Hudgins et al. (1994), Mattioda et al. (2005, 2017), Bouwman et al. (2011), and de Barros et al. (2017). First, at a temperature of 20 K, argon and IVA are codeposited (at an argon to IVA ratio of 8000 to 1, respectively) keeping the dominant IVA IR bands within an FWHM of 2 to 4  $\text{cm}^{-1}$ . The sample was then irradiated for 2, 4, 8, 16, and 32 minutes by UV photons. Infrared spectra were collected at no irradiation (neutral bands) and after every irradiation interval (ion bands) to monitor the evolution of IVA and its ions under a UV field. A second experiment was conducted in which the argon was doped with NO<sub>2</sub> (at an argon to NO<sub>2</sub> ratio of 2000 to 1, respectively, respectively) to matrix isolate the IVA, repeating the process as mentioned earlier, and preventing the formation of anions. A third experiment was conducted in a water matrix putting our results in an astrophysical context; water was used to understand the photochemistry of it with IVA (Bouwman et al. 2011; Cook et al. 2015; de Barros et al. 2017).

The column densities were calculated from their infrared absorption using the formula

$$N = \frac{1}{\mathcal{A}} \int_{\text{band}} \tau_\nu d\nu, \quad (2)$$

where,  $N$  is the column density in molecules per  $\text{cm}^2$ ,  $\mathcal{A}$  the band strength (*A*-values) in  $\text{cm molecule}^{-1}$ ,  $\tau_\nu$  the optical depth of the band, and  $d\nu$  the wavenumber differential. The adopted *A*-value for water was  $2 \times 10^{-16} \text{ cm molecule}^{-1}$  for its main band, the O–H stretch centered around  $3300 \text{ cm}^{-1}$  (d’Hendecourt & Allamandola 1986). The O–H bending ( $1660 \text{ cm}^{-1}$ ) and libration ( $760 \text{ cm}^{-1}$ ) modes were not used for the calculations since they overlap with the dominant IVA bands.

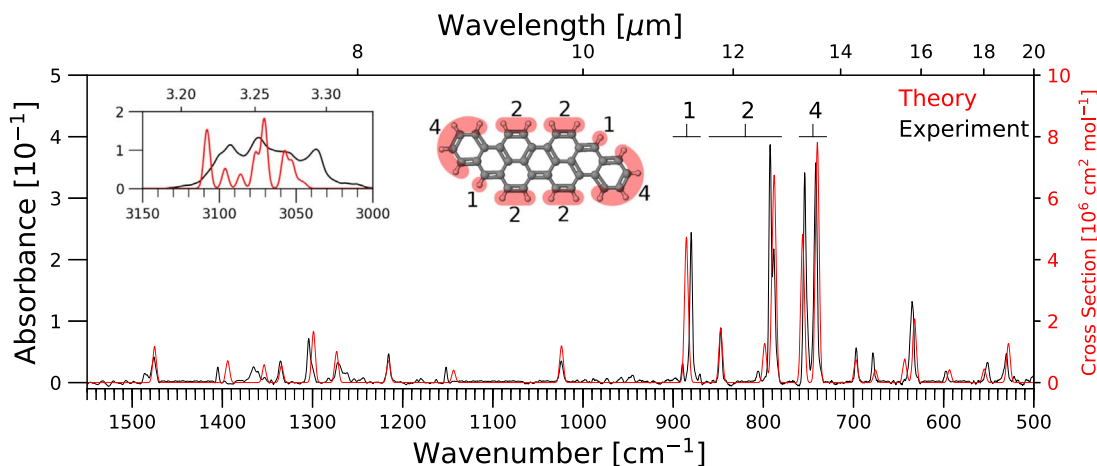


**Figure 2.** FTIR spectrum of IVA in an argon matrix (8000 to 1 ratio in black) compared to the computed IR spectrum of neutral IVA (red). The inset shows the 3  $\mu\text{m}$  region where the aromatic C–H stretching bands appear. The IVA molecular structure is depicted along with the solo (1), duo (2), and quartet (4) adjacent C–H groups. The experimental spectra have been normalized to  $1 \times 10^{15}$  molecules.

The thin-film experiments were done by depositing IVA on a CsI window. They were irradiated with UV photons at 20 K. Two IVA films were irradiated for intervals of 2, 4, 8, 16, 32, and 64 minutes. Two more samples were irradiated for longer intervals: 48, 144, and 192 hr. Soft electrons, with an energy of 1.5 keV, were used to bombard the IVA thin-film samples. These samples were exposed for periods of 10, 30, 60, 120, and 240 minutes, 24, and 48 hr. For hydrogen ( $\text{H}^+$ ) and helium ( $\text{He}^+$ ) bombardment, IVA was deposited on KBr windows and shipped to the Pontifical Catholic University of Rio de Janeiro where, inside a high-vacuum chamber, IVA was bombarded using a Van de Graaff accelerator; see Pilling et al. (2013). Hydrogen and helium ion beams with an energy of 1.5 MeV and fluxes of  $1.3 \times 10^{12}$  ions  $\text{cm}^{-2} \text{s}^{-1}$  and  $6.3 \times 10^{12}$  ions  $\text{cm}^{-2} \text{s}^{-1}$ , respectively, were used.

The geometry optimization and the harmonic frequency calculations were performed using density functional theory. The hybrid B3LYP functional in conjunction with the cc-pVTZ basis set and the Gaussian 09 suite of programs were used. The computed harmonic frequencies were scaled to lower frequencies using three scaling factors: 0.964 for C–H stretches, 0.979 for the 2500–1110  $\text{cm}^{-1}$  region, and 0.975 for the region greater than 1110  $\text{cm}^{-1}$ . The scaling factor was obtained based on data from Behlen et al. (1981), Pirali et al. (2009), and Cané et al. (1997). The integrated band intensities, in  $\text{km mol}^{-1}$ , were broadened in wavenumber space by 5  $\text{cm}^{-1}$  to produce synthetic spectra that were comparable to experimental bandwidths. The calculations did not include overtones, combination bands, and resonances, which are expected to be weak compared to fundamentals. The vibrational modes were visualized using the interactive molecular graphics tool Jmol.<sup>7</sup>

### 3. Experimental Results

#### 3.1. Matrix-isolation Experiments

##### 3.1.1. Argon Matrix

Figure 2 compares the IR experimental spectrum of IVA in an argon matrix at 20 K before irradiation (neutral bands) with the computed IR spectrum of neutral IVA. Experiments with different Ar to IVA ratios were performed, and some potential

contamination bands were noticed. These bands were identified as they did not increase with the IVA column density. These bands were removed from the spectrum in Figure 2 by subtracting two spectra with different column densities of IVA, providing a clean IVA spectrum. Baseline correction was performed, and the spectrum was normalized to  $1 \times 10^{15}$  molecules for presentation purposes. However, all measurements and calculations were performed using unaltered data.

When comparing experiments to theory, the agreement is good from 1000 to 500  $\text{cm}^{-1}$  for both peak positions and intensities. This agreement is somewhat less from 1500 to 1000  $\text{cm}^{-1}$  but in line with previous works (de Barros et al. 2017). The most intense IR bands of IVA are located between 1000 and 700  $\text{cm}^{-1}$  (10 to 14.28  $\mu\text{m}$ ) and are due to the C–H out-of-plane (C–Hoop) bending modes. A-values were determined using the theoretical absolute band intensities for IVA. The total theoretically calculated absolute intensity from 1600 to 500  $\text{cm}^{-1}$  was proportionally divided over the experimentally measured PAH band areas in the frequency range mentioned above, utilizing the relative intensities of the band areas (Mattioda et al. 2003, 2017; de Barros et al. 2017). Equation (3) was used to compute the experimental A-values:

$$\mathcal{A}_x^{\text{exp}} = I_x^{\text{exp}} \frac{\sum_{\nu=500}^{1600} \mathcal{A}^{\text{theory}}}{\sum_{\nu=500}^{1600} I^{\text{exp}}}, \quad (3)$$

where  $\mathcal{A}_x^{\text{exp}}$  and  $I_x^{\text{exp}}$  are the A-value and band integration of the  $x$ th band in the experimental data, respectively.  $\sum \mathcal{A}^{\text{theory}}$  is the summation over all theory A-values from 1600 to 500  $\text{cm}^{-1}$ , and  $\sum I^{\text{exp}}$  is the summation over all experimental bands in the same spectral range. This method produces A-values that vary by at most 20% (Mattioda et al. 2003). A column density of  $N = 5.2 \times 10^{16}$  molecules  $\text{cm}^{-2}$  was calculated for the neutral IVA. In the case of solid Ar, due to the lack of IR active modes, its thickness was measured using its fringe pattern as described in Section 3.2. A thickness of 170  $\mu\text{m}$  was measured.

The experimental and theoretical band positions, intensities, and band assignments are given in Table 1. Most of the experimental and theoretical bands are in good agreement except for the 632.2 and 643.0  $\text{cm}^{-1}$  bands where theory predicts two

<sup>7</sup> <http://jmol.sourceforge.net>

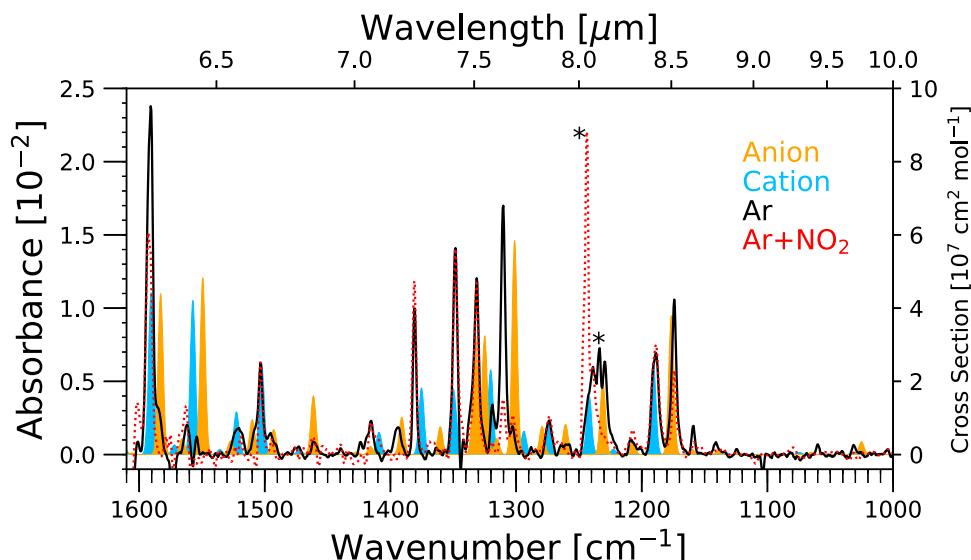


**Figure 3.** Difference spectra of UV-irradiated IVA in an argon matrix (black) and UV-irradiated IVA in a  $\text{NO}_2$  doped argon matrix (red); left y axis. The filled spectra are the theoretical spectra for  $\text{IVA}^+$  (cyan) and  $\text{IVA}^-$  (yellow), respectively; right y axis. Asterisks indicate the  $\text{NO}_2$  and Ar photoproducts. The experimental spectra have been normalized to  $1 \times 10^{15}$  molecules.

**Table 1**  
Neutral Band Positions and A-values for IVA in an Argon Matrix

	Theory			Experiment			Band Assignment
	Position ( $\text{cm}^{-1}$ )	Relative Intensity	Intensity ( $\text{Km mole}^{-1}$ )	Position ( $\text{cm}^{-1}$ )	Relative Intensity	A-value ( $\text{Km mole}^{-1}$ )	
Neutral Bands	528.1	0.16	12.7	529.9	0.10	9.2	$b_u$ skeletal in-plane bending
	554.9	0.05	4.4	551.1	0.07	5.5	$b_u$ skeletal in-plane bending
	593.5	0.05	4.1	597.4	0.04	2.8	$b_u$ skeletal in-plane bending
	632.2	0.26	20.7	634.5 <sup>a</sup>	0.31	21.2	$b_u$ skeletal in-plane bending
	643.0	0.09	7.7	...	...	...	$a_u$ skeletal out-of-plane bending
	675.7	0.05	4.1	677.9	0.13	5.7	$a_u$ skeletal out-of-plane bending
	697.2	0.09	7.4	697.2	0.14	8.5	$a_u$ skeletal out-of-plane bending
	740.1	1.00	78.1	741.6	0.73	69.9	$a_u$ C-H out-of-plane bending
	756.3	0.61	48.2	754.1	0.81	57.1	$a_u$ C-H out-of-plane bending
	787.5	0.86	55.8	787.9	0.48	50.6	$b_u$ skeletal in-plane bending
	789.8	0.25	19.7	792.5	1.00	75.4	$a_u$ C-H out-of-plane bending
	798.5	0.16	12.7	805.5	0.04	3.1	$a_u$ C-H out-of-plane bending
	847.2	0.22	17.5	846.7	0.20	12.9	$a_u$ C-H out-of-plane bending
	883.7	0.10	8.4	880.0	0.58	44.6	$a_u$ C-H out-of-plane bending
	885.5	0.52	41.3	889.6	0.09	5.0	$a_u$ C-H out-of-plane bending
	1023.8	0.15	11.9	1024.1	0.07	7.0	$b_u$ C-H in-plane bending
	1143.4	0.05	4.0	1151.9	0.06	3.8	$b_u$ C-H in-plane bending
	1215.4	0.09	7.1	1215.6	0.11	7.6	$b_u$ C-H in-plane bending
	1273.2	0.12	10.1	1272.0	0.06	5.7	$b_u$ C-H in-plane bending
	1298.9	0.21	16.6	1304.3	0.16	19.0	$b_u$ C-H in-plane bending
	1334.3	0.07	5.6	1335.0	0.04	2.5	$b_u$ C-H in-plane bending
	1353.6	0.09	5.8	1365.3	0.05	3.6	$b_u$ C-H in-plane bending
	1394.0	0.09	7.1	1405.0	0.03	2.3	$b_u$ C-H in-plane bending
	1475.1	0.15	11.7	1476.0	0.09	8.6	$b_u$ C-H in-plane bending
	3140-3000	0.80	279.2	3140-3000	0.12	213.2	aromatic C-H stretching

**Note.** Comparison between experiment and theory.

<sup>a</sup> Contribution from two bands.

bands; experiments show that they are blended into one at  $634.5 \text{ cm}^{-1}$ . Most experimental bands are within  $10 \text{ cm}^{-1}$  of their theoretical counterpart, except for  $1353.6$  and  $1394.0 \text{ cm}^{-1}$ , which vary by  $11.7$  and  $11.0 \text{ cm}^{-1}$ , respectively. This variation is similar to what we have observed in past experiments.

Matrix-isolated neutral IVA was then irradiated using  $\text{Ly}\alpha$  photons to ionize it. The most intense ionic modes fall in the  $1600\text{--}1000 \text{ cm}^{-1}$  region, in contrast to the neutral most intense modes that are in the  $1000\text{--}700 \text{ cm}^{-1}$  region; see Figure 3. Figure 3 shows the IR spectra of ionized IVA in an argon



**Table 2**  
Experimental and Theoretical Band Positions and Intensities for IVA<sup>+</sup> and IVA<sup>-</sup> in an Argon Matrix

	Theory		Experiment		Band Assignment
	Position (cm <sup>-1</sup> )	Intensity (Km mole <sup>-1</sup> )	Position (cm <sup>-1</sup> )	A-value (Km mole <sup>-1</sup> )	
<b>Cation Bands</b>					
	1162.3	6.8	1158.9 <sup>a</sup>	56.0	b <sub>u</sub> C-H in-plane bending
	1176.2	50.2	1174.1 <sup>a</sup>	445.6	b <sub>u</sub> C-H in-plane bending
	1190.8	254.1	1188.4	295.0	b <sub>u</sub> C-H in-plane bending
	1222.6	14.5	1208.0 <sup>a</sup>	25.0	b <sub>u</sub> C-H in-plane bending
	1241.8	158.8	1239.0	139.7	b <sub>u</sub> C-H in-plane bending
	1274.5	86.8	1273.2	84.3	b <sub>u</sub> C-H in-plane bending
	1293.7	63.7	1302.5	21.0	b <sub>u</sub> C-H in-plane bending
	1320.2	231.1	1310.5 <sup>a</sup>	782.8	b <sub>u</sub> C-H in-plane bending
	1333.1	162.6	1331.1	355.2	b <sub>u</sub> C-H in-plane bending
	1348.1	70.8	1348.5 <sup>b</sup>	457.6	b <sub>u</sub> C-H in-plane bending
	1350.7	143.7	b	...	b <sub>u</sub> C-H in-plane bending
	1375.2	182.1	1380.8	246.9	b <sub>u</sub> C-H in-plane bending
	1409.1	60.8	1415.5	39.7	b <sub>u</sub> C-H in-plane bending
	1502.4	245.3	1503.1	204.7	b <sub>u</sub> C-H in-plane bending
	1522.5	116.4	1521.0 <sup>a</sup>	81.2	b <sub>u</sub> C-H in-plane bending
	1557.2	420.7	1562.5 <sup>a</sup>	91.1	b <sub>u</sub> C-C stretching
	1590.4	441.7	1592.5 <sup>a</sup>	843.0	b <sub>u</sub> C-C stretching
<b>Anion Bands</b>					
	1160.0	14.3	1158.9 <sup>a</sup>	56.0	b <sub>u</sub> C-H in-plane bending
	1176.4	379.0	1174.1 <sup>a</sup>	445.6	b <sub>u</sub> C-H in-plane bending
	1207.2	36.7	1208.0 <sup>a</sup>	25.0	b <sub>u</sub> C-H in-plane bending
	1230.9	199.6	1229.4	168.6	b <sub>u</sub> C-H in-plane bending
	1260.6	82.6	1258.3	10.1	b <sub>u</sub> C-H in-plane bending
	1279.3	76.6	1289.5	8.1	b <sub>u</sub> C-H in-plane bending
	1301.2	583.8	1310.5 <sup>a</sup>	782.8	b <sub>u</sub> C-H in-plane bending
	1324.9	323.7	1319.3 <sup>b</sup>	72.2	b <sub>u</sub> C-H in-plane bending
	1332.5	330.0	b	...	b <sub>u</sub> C-H in-plane bending
	1360.3	75.8	c	...	b <sub>u</sub> C-H in-plane bending
	1390.9	101.7	1393.0	78.2	b <sub>u</sub> C-H in-plane bending
	1415.7	21.7	1419.0	22.9	b <sub>u</sub> C-H in-plane bending
	1461.3	160.4	c	...	b <sub>u</sub> C-H in-plane bending
	1492.8	68.3	1495.6	25.1	b <sub>u</sub> C-H in-plane bending
	1509.9	95.1	1505.0	21.3	b <sub>u</sub> C-H in-plane bending
	1527.2	37.1	1521.0 <sup>a</sup>	81.2	b <sub>u</sub> C-H in-plane bending
	1549.3	482.9	1562.5 <sup>a</sup>	91.1	b <sub>u</sub> C-C stretching
	1582.8	439.0	1592.5 <sup>a</sup>	843.0	b <sub>u</sub> C-C stretching

**Notes.**<sup>a</sup> Contribution from two bands, one from each ion.<sup>b</sup> Contribution from two bands of the same ion.<sup>c</sup> Bands with no assignment.

matrix as well as an argon matrix doped with NO<sub>2</sub>. In Figure 3, a clear separation between the black spectrum (pure Ar) and the red spectrum (NO<sub>2</sub> doped Ar) can be observed in some bands; this is an indication that, at that position, there is an IVA<sup>-</sup> mode (e.g., bands centered at 1174.1, 1229.4, and 1310.5 cm<sup>-1</sup>).

Cation and anion modes were assigned by comparing the argon and argon-doped experiments and theory. The theoretical data for IVA cation and anion modes are represented as the blue (IVA<sup>+</sup>) and yellow (IVA<sup>-</sup>) filled spectra, respectively, in Figure 3. In Table 2, we report the experimental and theoretical band positions as well as intensities of IVA<sup>+</sup> and IVA<sup>-</sup>. Cation and anion modes overlap in all the spectral ranges; experimental bands like 1158.9, 1174.1, 1208.0, 1310.5, 1521.0, 1562.5, and 1592.5 cm<sup>-1</sup> do not correlate entirely with theory since it does not account for band overlap. The same case

applies to two bands of the same ion that are too close to each other: cation theoretical bands centered at 1348.1 and 1350.7 cm<sup>-1</sup> are blended into one at 1348.5 cm<sup>-1</sup> in the case of experimental data. IVA<sup>-</sup> modes predicted at 1360.3 and 1461.3 cm<sup>-1</sup> by theory do not have a clear assignment. While the 1360.3 cm<sup>-1</sup> mode could overlap with the 1348.5 cm<sup>-1</sup> experimental band, the 1461.3 cm<sup>-1</sup> mode could be too weak to stand out from background noise.

3.1.2. H<sub>2</sub>O Matrix

Water-matrix experiments were performed to understand the interaction of H<sub>2</sub>O (a ubiquitous molecule in space) and PAHs. IVA was deposited in a water matrix at 20 K with ratios of 10:1, 100:1, and 150:1 [H<sub>2</sub>O:PAH]. Upon analysis, the same photoproducts bands were observed among the three ratios;

**Table 3**  
Neutral Band Positions and Intensities for IVA in an Argon Matrix and in a Water Matrix

Ar Matrix		Water Matrix	
Position (cm <sup>-1</sup> )	A-value (Km mole <sup>-1</sup> )	Position (cm <sup>-1</sup> )	A-value (Km mole <sup>-1</sup> )
529.9	9.2	530.8	7.6
551.1	5.5	553.9	4.5
597.4	2.8	597.4	2.3
634.5	21.2	632.6	17.5
677.9	5.7	677.4	4.7
697.2	8.5	696.2	7.0
741.6	69.9	744.9	57.8
754.1	57.1	754.4	47.2
787.9	50.6	791.2*	70.2
792.5	75.4	*	...
805.5	3.1	808.7	2.5
846.7	12.9	848.6	10.6
880.0	44.6	879.3	36.8
889.6	5.0	888.1	4.1
1024.1	7.0	1023.6	5.9
1151.9	3.8	1150.8	3.0
1215.6	7.6	1215.4	6.5
1272.0	5.7	1272.3	3.9
1304.3	19.0	1301.8	15.6
1335.0	2.5	1335.5	1.5
1365.3	3.6	1366.7	3.5
1405.0	2.3	1401.0	1.8
1476.0	8.6	1474.5	6.5

therefore, here, we provide data and analysis for the 100:1 ratio. This behavior is similar to the one reported by Bouwman et al. (2011), Cook et al. (2015), and de Barros et al. (2017). They noticed an inflection point at the 300:1 [H<sub>2</sub>O:PAH] ratio where below this concentration PAH ion-driven and ion-dominated chemical reactions are favored while for higher concentrations chemical reactions are mostly dominated by neutral species. For this experiment, IVA has a column density of  $5.1 \times 10^{16}$  molecules cm<sup>-2</sup> and water a column density of  $4.9 \times 10^{18}$  molecules cm<sup>-2</sup> (about 1.5 μm).

The aromatic or C–H stretching PAH region from 3200 to 3000 cm<sup>-1</sup> is profoundly impacted by the O–H stretching mode of water; therefore, we do not report measurements and calculations obtained from this area. Moreover, from 1000 to 500 cm<sup>-1</sup> the H–O–H bending mode of water dominates the spectrum, which affects the most active neutral bands of IVA by broadening and blending them, making the band identification and subsequent integration difficult. For this reason, bands between 1600 and 1000 cm<sup>-1</sup> are those used to measure the PAH column density as they have minimal overlap with H<sub>2</sub>O; see de Barros et al. (2017) and Bouwman et al. (2011). Experiments were performed using the same protocol as for the argon-matrix experiments. Band assignments for IVA in the water matrix are reported in Table 3. In general, the IVA bands are broader compared to the IVA bands in the argon matrix. The bands at 787.9 and 792.5 cm<sup>-1</sup> in the argon matrix are blended into one at 791.2 cm<sup>-1</sup> in the water matrix.

The A-values for the IVA neutral bands in the water matrix were calculated following the procedure described in de Barros et al. (2017). Since the water absorption bands centered at 3277, 1660, and 750 cm<sup>-1</sup> dominate the mid-IR spectrum, the region between 1500 and 1000 cm<sup>-1</sup> was chosen for the

calculations. A-values in this range were calculated, see Table 3, and they were compared to the A-values in the argon matrix. An average 17% decrease in intensity for the A-values in the water matrix was found compared to the A-values in the argon matrix. This result is in agreement with de Barros et al. (2017), who found a 15% decrease in their experiments.

IVA prefers to undergo addition or substitution at its solo positions (see position 1 in Figure 2). These positions are preferred for atoms or molecular groups like hydrogen, oxygen, and the hydroxyl radical to form new species. Protonated IVA (IVH), IVA alcohol (IVHOH), and IVA quinone (IVO), as well as IVA<sup>+</sup>, have been considered as the most likely molecules to be produced by photolysis due to the fact that UV photons (10.2 eV) are able to dissociate water molecules into H + OH, and at some extent, produce oxygen atoms.

Figure 4 shows the spectrum of IVA in a water matrix after 8 minutes of UV irradiation with the IVA neutral bands subtracted (black trace) together with the theoretical spectra of the potential photoproducts. The theoretical data have not been scaled for plotting purposes permitting comparisons among them. The purple, blue, and yellow spectra represent the theoretical spectra for IVH/IVH<sup>+</sup>, IVHOH/IVOH<sup>+</sup>, and IVO/IVO<sup>+</sup>, respectively. These molecules are shown at the bottom of Figure 4. The spectrum of IVA<sup>+</sup> is shown in gray.

The identification of photoproducts was made by correlating experimental bands with the most likely carrier from theoretical calculations. Band positions and intensities are reported in Table 4. Photoproduct bands from 1000 to 500 cm<sup>-1</sup> are not included because the water bending mode dominates. It is worth noticing that new photoproduct bands are difficult to assign in this region since, besides the broad water band, IVA neutral bands dominate this spectral region.

H<sub>2</sub>O, like NO<sub>2</sub>, can act as an electron acceptor, and for this reason, IVA anion modes were not identified in the water ice experiment. This statement is based on the lack of anion bands at positions marked as the red exclamation points (!) in Figure 4. There is not a clear band near 1158.9 cm<sup>-1</sup>, and the intensities of bands at 1174.1 and 1310.5 cm<sup>-1</sup> suggest a contribution only from cations. IVA<sup>+</sup> modes were already assigned in Section 3.1.1. Moreover, they are easy to spot by comparing theory and experiment in Figure 4. Contributions from IVA<sup>+</sup> modes can be observed at 1171.0, 1187.9, 1317.4, 1333.5, and 1348.5 cm<sup>-1</sup> and partial contribution from IVA<sup>+</sup> modes can be seen at 1270.7, 1282.4, 1499.1, and 1589.9 cm<sup>-1</sup>; see the gray crosses in Figure 4.

Blue asterisks represent bands with a contribution from IVHOH<sup>+</sup> in Figure 4. Contributions from IVHOH<sup>+</sup> bands are observed at 1602.2, 1574.1 (the most intense band in the experimental spectrum), 1471.1, 1412.3, and 1199.3 cm<sup>-1</sup> and bands in the 1390–1360 cm<sup>-1</sup> region. This assignment was made using the IVHOH<sup>+</sup> correlation plots in Figure 5 where bands grow at the same rate. Nevertheless, IVHOH has its most intense band at 1374.1 cm<sup>-1</sup>; this means that the experimental band at 1374.9 cm<sup>-1</sup> must have a substantial contribution from IVHOH considering how intense it is in the spectrum.

Purple asterisks represent bands with a contribution from IVH<sup>+</sup> in Figure 4. Contributions from IVH<sup>+</sup> bands are observed at 1512.5, 1489.5, 1420.1, 1401.2, 1303.8, and 1211.9 cm<sup>-1</sup>. This assignment was made using the IVH<sup>+</sup> correlation plots in Figure 5 where bands grow at the same rate. By looking at the overall intensities of IVH<sup>+</sup> modes in the experiment one can notice that IVH<sup>+</sup> modes are a bit weaker

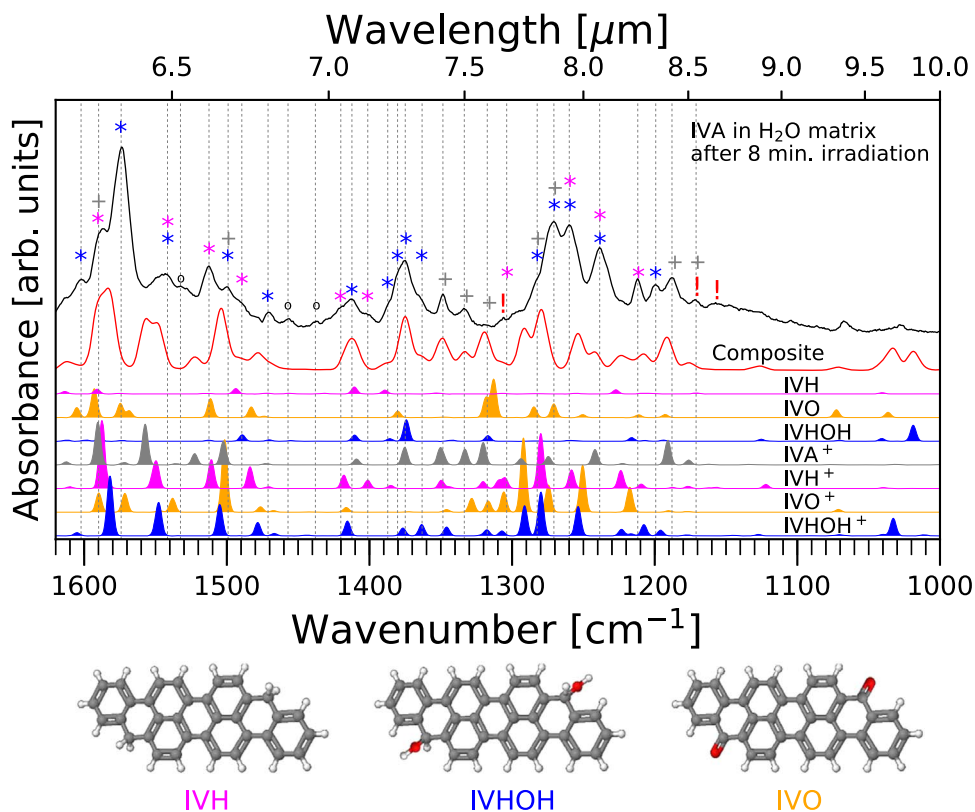


**Figure 4.** IR spectrum of IVA in water matrix after 8 minutes of UV irradiation (black). Neutral bands have been subtracted from the spectrum.  $\text{IVA}^+$  theory is in gray. IVH and  $\text{IVH}^+$  theory are in purple. IVHOH and  $\text{IVHOH}^+$  theory are in blue. IVO and  $\text{IVO}^+$  theory are in yellow. The red spectrum is the sum of the  $\text{IVA}^+$ , IVH,  $\text{IVH}^+$ , IVHOH, and  $\text{IVHOH}^+$  theoretical spectra. The lack of intense bands at positions marked as “!” indicates a lack of  $\text{IVA}^-$ . Bands marked as “o” in Figure 4 are bands with no specific assignment.

than  $\text{IVHOH}^+$ . IVH has the weakest modes of all of the theory data, and unlike IVHOH, no intense band can be assigned.

IVO is easy to rule out by looking at its most intense band at  $1312.8\text{ cm}^{-1}$ . There is no particularly intense band in this region. The most intense band for  $\text{IVO}^+$  peaks at  $1501.5\text{ cm}^{-1}$ . There is a band near this position, but the most probable candidates are  $\text{IVHOH}^+$  and  $\text{IVA}^+$ . Bands marked as o in Figure 4 are bands with no specific assignment. While bands centered at  $1457.1$  and  $1437.9\text{ cm}^{-1}$  could be linked to  $\text{IVHOH}^+$ , the band at  $1532.5\text{ cm}^{-1}$  has no clear carrier.

Correlation plots were used to verify whether photoproduct bands belonged to a particular photoproduct, because bands from the same molecule grow proportionally to each other, as evidenced by the linear relations among bands in Figure 5. Experimental bands were assigned to carriers using Figures 4, 5, and Table 4.

So far we have not mentioned the region from  $1300$  to  $1220\text{ cm}^{-1}$ , because, unlike in the rest of the spectral range, the experimental bands present an average redshift of  $18\text{ cm}^{-1}$  compared to the theoretical bands. The most intense bands in this region are centered at  $1270.7$ ,  $1259.9$ , and  $1238.6\text{ cm}^{-1}$ , and as shown in Figure 5, they are correlated.  $\text{IVHOH}^+$  would be the strongest candidate, but  $\text{IVH}^+$  cannot be ruled out since it has a strong band in this region. The fact that only this region is affected could indicate that it is susceptible to the influence of overlapping photoproduct bands, matrix effects, or hydrogenation of IVA molecules.

It is not surprising that  $\text{IVHOH}^+$  could be potentially the strongest photoproduct since the production of alcohols

is typical for UV-irradiated water-matrix-isolated PAHs. Bernstein et al. (1999, 2001, 2002) found that naphthalene in the water matrix produced naphthol and naphthoquinone molecules upon UV irradiation, with naphthol molecules being the most abundant. Moreover, Bouwman et al. (2011), Cook et al. (2015), and de Barros et al. (2017) reported the production of alcohol and protonated molecules as well as quinone photoproducts.

The  $\text{IVA}^+$ , IVHOH,  $\text{IVHOH}^+$ , and  $\text{IVH}^+$  theoretical spectra were summed into one in an attempt to recreate the experimental spectrum (see the red spectrum in Figure 4).

Photoproducts like  $\text{H}_2\text{O}_2$  ( $2850\text{ cm}^{-1}$ ), as well as  $\text{CO}_2$  ( $2345\text{ cm}^{-1}$ ), were detected growing in the infrared spectrum. Using Gerakines et al. (1995) and Moore & Hudson (2000) values for the  $\text{CO}_2$  and  $\text{H}_2\text{O}_2$  A-values, a column density of  $4.6 \times 10^{14}\text{ molecules cm}^{-2}$  for  $\text{CO}_2$  and a column density of  $1.2 \times 10^{15}\text{ molecules cm}^{-2}$  for  $\text{H}_2\text{O}_2$  were calculated after a UV dose of 32 minutes ( $3.84 \times 10^{17}\text{ photons cm}^{-2}$ ). It is a total production of 0.07% of  $\text{CO}_2$  with respect to water and 0.9% of  $\text{CO}_2$  with respect to neutral IVA. In the case of hydrogen peroxide, a production of 0.2% of  $\text{H}_2\text{O}_2$  with respect to water was measured.

### 3.2. Thin-film Experiments

IVA was also deposited as a thin film by sublimating the IVA directly on top of KBr and CsI windows. Due to intermolecular interactions, solid IVA exhibits much broader bands than matrix-isolated IVA; see Figure 6. The film

**Table 4**  
Photoproduct Bands for IVA in a Water Matrix under a UV Field

Experiment		Theory													
IVA+H <sub>2</sub> O		IVA <sup>+</sup>		IVHOH		IVHOH <sup>+</sup>		IVH		IVH <sup>+</sup>		IVO		IVO <sup>+</sup>	
Position (cm <sup>-1</sup> )	Relative Intensity	Position (cm <sup>-1</sup> )	Intensity (Km mole <sup>-1</sup> )	Position (cm <sup>-1</sup> )	Intensity (Km mole <sup>-1</sup> )	Position (cm <sup>-1</sup> )	Intensity (Km mole <sup>-1</sup> )	Position (cm <sup>-1</sup> )	Intensity (Km mole <sup>-1</sup> )	Position (cm <sup>-1</sup> )	Intensity (Km mole <sup>-1</sup> )	Position (cm <sup>-1</sup> )	Intensity (Km mole <sup>-1</sup> )	Position (cm <sup>-1</sup> )	Intensity (Km mole <sup>-1</sup> )
1025.5	0.04	...	...	1018.7	165.2	1032.7	181.3	1040.6	12.9	1039.7	10.2	1036.4	54.5	...	...
1068.1	0.13	...	...	1070.3	9.2	1069.3	9.8	...	...	...	...	1072.6	80.8	1071.2	29.0
1171.0	0.10	1176.2	50.2	...	...	1195.8	58.7	1170.8	10.5	1176.6	23.6	...	...	...	...
1187.9	0.22	1190.8	254.1	1193.9	11.5	1207.5	116.3	...	...	1187.6	11.4	1192.7	32.3	...	...
1199.3	0.09	...	...	1207.0	7.7	1216.4	16.6	...	...	1209.4	45.8	...	...	...	...
1211.9	0.17	...	...	1216.1	31.5	1223.2	67.3	1207.5	10.1	1223.7	186.4	1211.2	29.7	1217.4	258.3
1238.6	0.38	1241.8	158.8	...	...	1253.7	303.1	1227.2	42.9	1258.3	193.2	...	...	1250.5	485.0
1259.9	0.48	...	...	1260.1	10.0	1279.7	451.8	1255.0	7.1	...	...	1250.4	31.2	1274.5	281.0
1270.7	0.51	1274.5	86.8	...	...	1291.2	311.4	...	...	1279.8	569.1	1270.7	141.9	1292.0	767.3
1282.4	0.16	...	...	1281.2	5.5	...	...	1280.9	4.8	...	...	1284.6	110.7	...	...
1303.8	0.12	1293.7	63.7	...	...	1307.1	50.8	1306.5	6.8	1304.8	106.6	...	...	1305.8	209.8
1317.4	0.02	1320.2	231.1	...	...	1317.6	61.8	...	...	1309.4	80.6	1312.8	393.3	1316.6	115.5
1333.5	0.15	1333.1	162.6	...	...	...	...	...	...	...	...	...	...	1328.3	143.5
1348.5	0.24	1350.7	143.7	1342.1	12.3	1345.9	91.1	1352.8	11.8	1349.6	85.4	1347.8	6.1	1345.9	27.6
1363.1	0.16	...	...	...	...	1363.3	117.0	...	...	...	...	...	...	...	...
1374.9	0.52	1375.2	182.1	1374.1	221.9	1376.5	81.0	...	...	...	...	...	...	1372.3	4.7
1380.3	0.49	...	...	...	...	...	...	...	...	...	...	1380.1	65.5	...	...
1387.2	0.15	...	...	1385.7	26.6	...	...	1389.1	39.7	1385.0	32.4	...	...	...	...
1401.2	0.07	...	...	...	...	...	...	...	...	1401.2	85.8	...	...	...	...
1412.3	0.24	1409.1	60.8	1410.4	63.6	1415.4	153.0	1410.5	71.8	...	...	...	...	1416.2	48.8
1420.1	0.13	...	...	...	...	...	...	...	...	1417.9	138.7	...	...	...	...
1437.9	0.06	...	...	...	...	...	...	1431.3	6.4	...	...	...	...	...	...
1457.1	0.07	...	...	1455.0	7.3	...	...	1456.4	7.2	...	...	...	...	1467.2	16.8
1471.1	0.08	...	...	1470.3	14.6	1478.3	138.3	1471.7	8.8	1470.8	18.9	1473.9	14.3	1476.4	55.7
1489.5	0.09	...	...	1489.1	66.3	...	...	...	...	1483.7	224.8	1482.8	110.2	...	...
1499.1	0.17	1502.4	245.3	...	...	...	...	1493.7	55.3	...	...	...	...	1501.5	750.2
1512.5	0.24	...	...	1512.7	11.1	1504.9	323.7	1514.3	6.8	1510.8	299.0	1511.4	196.1	...	...
1532.5	0.11	...	...	...	...	...	...	...	...	...	...	...	...	1538.0	144.2
1542.6	0.25	1557.2	420.7	...	...	1547.4	288.8	...	...	1549.0	230.5	...	...	1547.1	16.8
1574.1	1.00	...	...	1573.4	8.6	1582.1	489.8	1575.0	6.4	1587.6	699.5	1574.6	147.2	1571.5	194.3
1589.9	0.34	1590.4	441.7	1589.1	25.9	...	...	1590.9	48.7	...	...	1592.7	273.4	1589.7	198.9
1602.2	0.09	...	...	1597.9	8.4	1605.1	33.4	1613.5	26.0	1610.0	18.6	1605.1	103.5	...	...



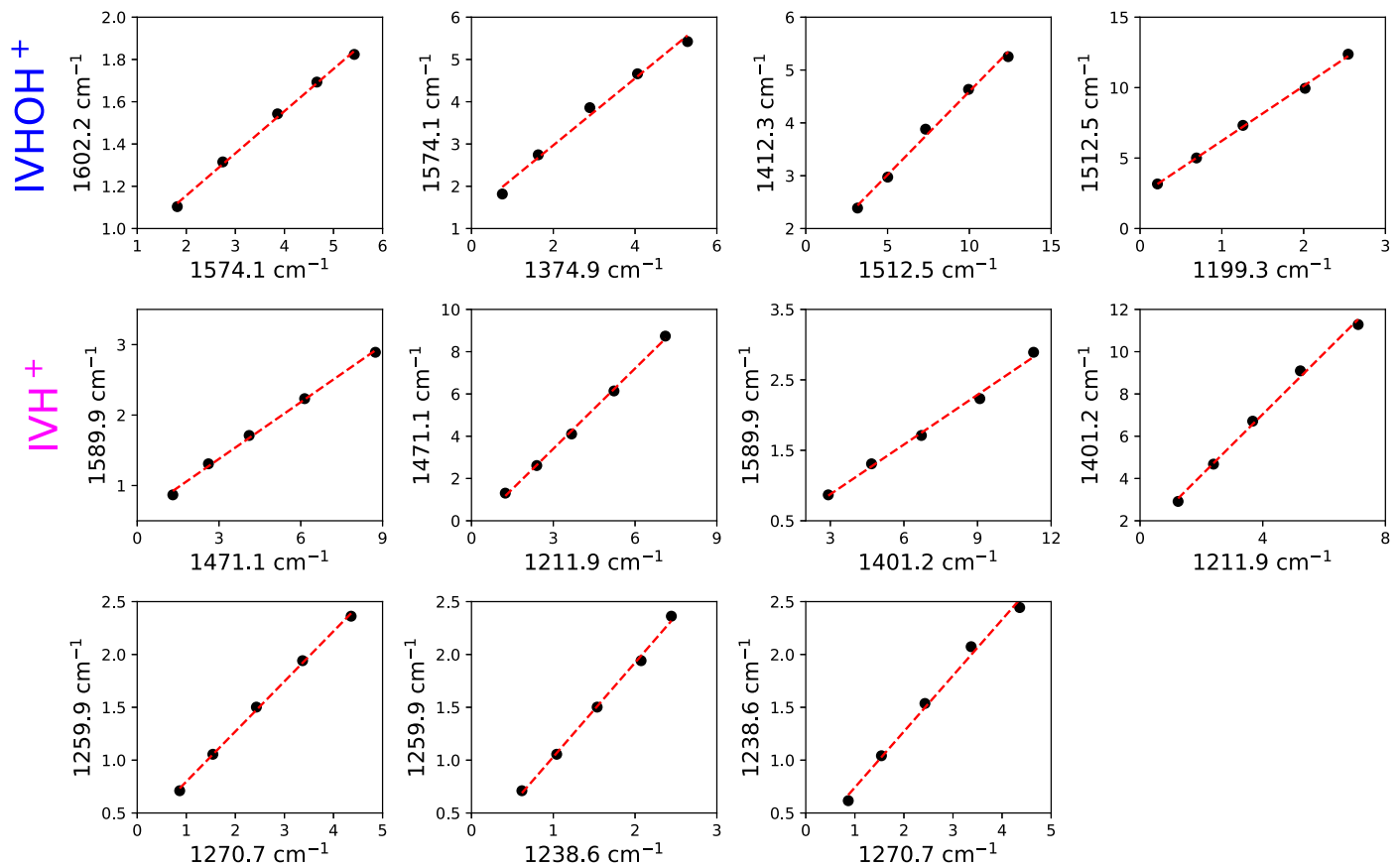


Figure 5. Correlation plots for some of the most intense bands of IVOH<sup>+</sup> and IVH<sup>+</sup>.

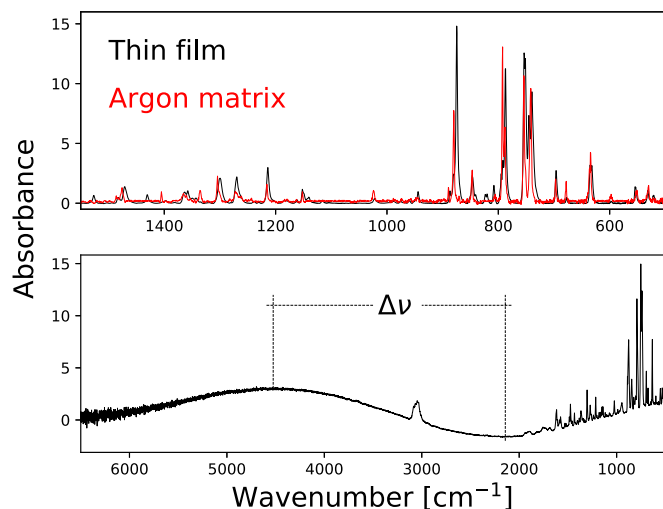


Figure 6. IR spectrum of IVA as a thin film showing the fringe pattern used for the determination of film thickness. The experimental spectra have been normalized to  $1 \times 10^{15}$  molecules.

thickness was calculated following the classical inter-fringe relation

$$d = \frac{1}{2n \cdot 2(\Delta\nu)}, \quad (4)$$

where  $d$  is the thickness of the film,  $n$  is the refractive index of the IVA (2.030; <http://www.chemspider.com>), and  $\Delta\nu$  is the wavenumber difference between an adjacent maximum and

minimum of the fringes observed in the infrared spectrum; see Figure 6. Using this relation, the column density and, subsequently, the A-values (see Table 5) were calculated for the solid phase using

$$N = N_A d \frac{\rho}{m}, \quad (5)$$

where  $N$  is the column density,  $N_A$  the Avogadro constant,  $\rho$  the density of IVA ( $1.4 \text{ g cm}^{-3}$ ; <http://www.chemspider.com>), and  $m$  the molar mass of IVA ( $426.507 \text{ g mol}^{-1}$ ). On average, the thin films were deposited with a thickness of  $0.45 \pm 0.05 \mu\text{m}$ , which translates into a column density of  $1 \times 10^{17}$  molecules  $\text{cm}^{-2}$ .

The entire spectrum of the IVA thin film has been divided into four regions for analysis purposes: region 1, skeletal modes ( $700$  to  $500 \text{ cm}^{-1}$ ); region 2, C-Hoop modes ( $1000$  to  $700 \text{ cm}^{-1}$ ); region 3, C-C and C-H in-plane modes ( $1600$  to  $1000 \text{ cm}^{-1}$ ); region 4, C-H stretching modes ( $3200$  to  $2900 \text{ cm}^{-1}$ ). The average redshift of IVA thin film compared to IVA in an argon matrix for each region was measured to be  $1.0$ ,  $2.0$ ,  $1.5$ , and  $9.0 \text{ cm}^{-1}$ , respectively.

The IVA A-values for both phases (thin film and argon matrix) were correlated using linear regression. It has been found that the most intense bands located in the C-Hoop region presented a slope of  $[\text{Thin Film}]/[\text{Ar}] = 2.0$ , while bands in the skeletal and C-C and C-H in-plane regions presented a slope of  $[\text{Thin Film}]/[\text{Ar}] = 1.2$ . This result indicates that IVA C-Hoop modes are more affected in the solid state due to the interactions between adjacent molecules, as expected. After thin-film deposition, there was the presence of aliphatic bands

**Table 5**

Band Positions and A-values for IVA in an Argon Matrix Compared with Those of an IVA Thin Film

Argon Matrix		Thin Film		
Position ( $\text{cm}^{-1}$ )	A-value ( $\text{Km mole}^{-1}$ )	Position ( $\text{cm}^{-1}$ )	$\Delta\nu$ ( $\text{cm}^{-1}$ )	A-value ( $\text{Km mole}^{-1}$ )
529.9	9.2	531.6	+1.7	8.8
551.1	5.5	550.6	-0.5	8.5
597.4	2.8	597.3	-0.1	3.6
634.5	21.2	633.0	-1.5	23.6
677.9	5.7	677.4	-0.5	4.5
697.2	8.5	695.0	-2.2	16.4
741.6	69.9	739.6	-2.0	131.9
754.1	57.1	751.7	-2.4	119.2
787.9	50.6	784.9	-3.0	75.5
792.5	75.4	791.7	-0.8	62.8
805.5	3.1	804.2	-1.3	3.8
846.7	12.9	845.0	-1.7	21.1
880.0	44.6	876.4	-3.6	105.9
889.6	5.0	888.6	-1.0	22.0
1024.1	7.0	1023.0	-1.1	7.8
1151.9	3.8	1149.4	-2.5	6.5
1215.6	7.6	1214.4	-1.2	14.6
1272.0	5.7	1271.0	-1.0	8.5
1304.3	19.0	1302.6	-1.7	28.5
1335.0	2.5	1334.8	-0.2	3.0
1365.3	3.6	1366.0	+0.7	4.3
1405.0	2.3	1402.6	-2.4	3.8
1476.0	8.6	1473.7	-2.3	26.4
3140-3000	213.2	3120-2980	-9.0	221.0

in the spectrum. The presence of these bands did not affect the entire spectrum, nor the measurements and calculations made.

### 3.2.1. UV Irradiation of IVA Thin Films

As a thin film, IVA is very resilient to UV photons, with very little processing under UV light. No photoproduct or ion bands were observed, see Figure 7(A), where a total decrease of 1% in the IVA column density after 64 minutes and 7% after 192 hr of irradiation was measured. Using the UV fluence ( $1.38 \times 10^{20}$  photons  $\text{cm}^{-2}$ ) and mean energy mentioned of our UV lamp, the latter translates into a full energy dose of  $1.4 \times 10^{21}$  eV  $\text{cm}^{-2}$  for the longest irradiation. In the case of the long irradiation times, a broad feature between 1250 and  $950 \text{ cm}^{-1}$  ( $8.0$  to  $10.5 \mu\text{m}$ ) with a maximum at  $1040 \text{ cm}^{-1}$  ( $9.6 \mu\text{m}$ ) can be seen growing with increasing UV dose (see the green subtraction spectrum in Figure 7(A)). This broad feature can be fitted by three Gaussians centered at 1027 (most intense), 1110, and  $1190 \text{ cm}^{-1}$ . Vibrational bands in regions 1 to 3 were integrated and plotted as a function of the energy dose; see Figure 8(A). The IVA vibrational modes did not show any major decreasing under UV photolysis, making observations of any trend difficult.

### 3.2.2. Electron Bombardment of IVA Thin Films

No new bands were observed as a result of the electron bombardment; see Figure 7(B). An 18% column density decrease was measured after 60 minutes of bombardment and a 45% decrease after 48 hr; the latter can be translated into a total energy dose of  $7.8 \times 10^{23}$  eV  $\text{cm}^{-2}$ . As for UV-irradiated IVA thin films, a broad feature is observed growing as a function of bombardment time between  $1700$  and  $1030 \text{ cm}^{-1}$  ( $5.9$  to

$9.7 \mu\text{m}$ ), a smaller feature is also visible between  $1030$  and  $900 \text{ cm}^{-1}$  ( $9.7$  to  $11.1 \mu\text{m}$ ); see the subtraction in Figure 7(B). Gaussian fitting was performed with bands centered at 1550, 1420, 1300 (the most intense), 1100, and  $970 \text{ cm}^{-1}$ . Although similar to the broad UV feature, the electron bombardment feature is broader and more intense with a maximum at  $9.6 \mu\text{m}$ . Neutral IVA bands were integrated and plotted as a function of the energy dose in Figure 8(B). Regions 1 and 3 presented a slightly higher rate of decrease than region 2: on average a 55% decrease for regions 1 and 3 and a 45% decrease in the case of region 2 after 48 hr of bombardment. This result suggests the skeletal ( $700$  to  $500 \text{ cm}^{-1}$ ) and C-C and C-H in-plane modes ( $1600$  to  $1000 \text{ cm}^{-1}$ ) are more affected by electron bombardment producing a cross-linking effect among IVA molecules. A turning point after 240 minutes ( $6.5 \times 10^{22}$  eV  $\text{cm}^{-2}$ ) was observed in the data. This turning point is when regions start decreasing at different rates.

Kyriakou et al. (2013) calculated the electron penetration in multiwalled carbon nanotube materials for beam energies of  $\sim 0.3$  to  $30 \text{ keV}$  based on event-by-event Monte Carlo simulations. They gave the relation between the incident electron energy and the penetration depth of the target. Since PAHs are carbon-based molecules with a structure similar to carbon nanotubes, the same relation for estimating the penetration depth of electrons in IVA thin films were used. A penetration depth of  $\sim 21\%$  of the total thickness in IVA thin films (about  $0.1 \mu\text{m}$ ) was calculated. This result implies that soft electrons can process only the top layers of the IVA thin film to produce a broad feature.

### 3.2.3. Ion Bombardment of IVA Thin Films

$\text{H}^+$  particles with an energy of  $1.5 \text{ MeV}$  were used to process the IVA thin films. Samples were bombarded for a total of 83.2 minutes; see Figure 7(C). Although  $\text{H}^+$  particles were more efficient than UV photons or soft electrons in destroying the IVA, no broad or intense features were observed during or after the bombardment. This result suggests  $1.5 \text{ MeV } \text{H}^+$  has a different interaction mechanism with PAH than UV photons and soft electrons. After a total of 83.2 minutes of bombardment (an energy dose of  $9.7 \times 10^{21}$  eV  $\text{cm}^{-2}$ ), the IVA bands in regions 1 and 3 decreased an average of 40%, while bands in region 2 had a decrease of 20%. This result denotes a different rate of decrease for the regions, similar behavior to soft electron bombardment experiments. A turning point around 8.2 minutes of bombardment (energy dose of  $9.6 \times 10^{20}$  eV  $\text{cm}^{-2}$ ) was observed; see Figure 8(C). The energy dose required for the turning point is about two orders of magnitude lower compared to the electron-bombarded IVA.

$\text{He}^+$  particles with an energy of  $1.5 \text{ MeV}$  were used to bombard the IVA for up to 26.1 minutes, and again no new bands were observed; see Figure 7(D). After the samples were processed, a broad feature on region 1 centered at  $800 \text{ cm}^{-1}$  ( $12.5 \mu\text{m}$ ) was detected; see the Gaussian fit in Figure 7(D). It was noticed that IVA bands do not have the same response to high-energy processing, as in the case for soft electron and  $\text{H}^+$  particle bombardment. This time the effect is more noticeable for region 1 and region 3 since these bands disappeared after 26.1 minutes ( $1.5 \times 10^{22}$  eV  $\text{cm}^{-2}$ ) of  $\text{He}^+$  bombardment. On the other hand, bands in region 2 decreased an average of 60%. A turning point at 28 s ( $8.9 \times 10^{19}$  eV  $\text{cm}^{-2}$ ) was observed; see Figure 8(D). After  $\text{He}^+$  bombardment the four most intense

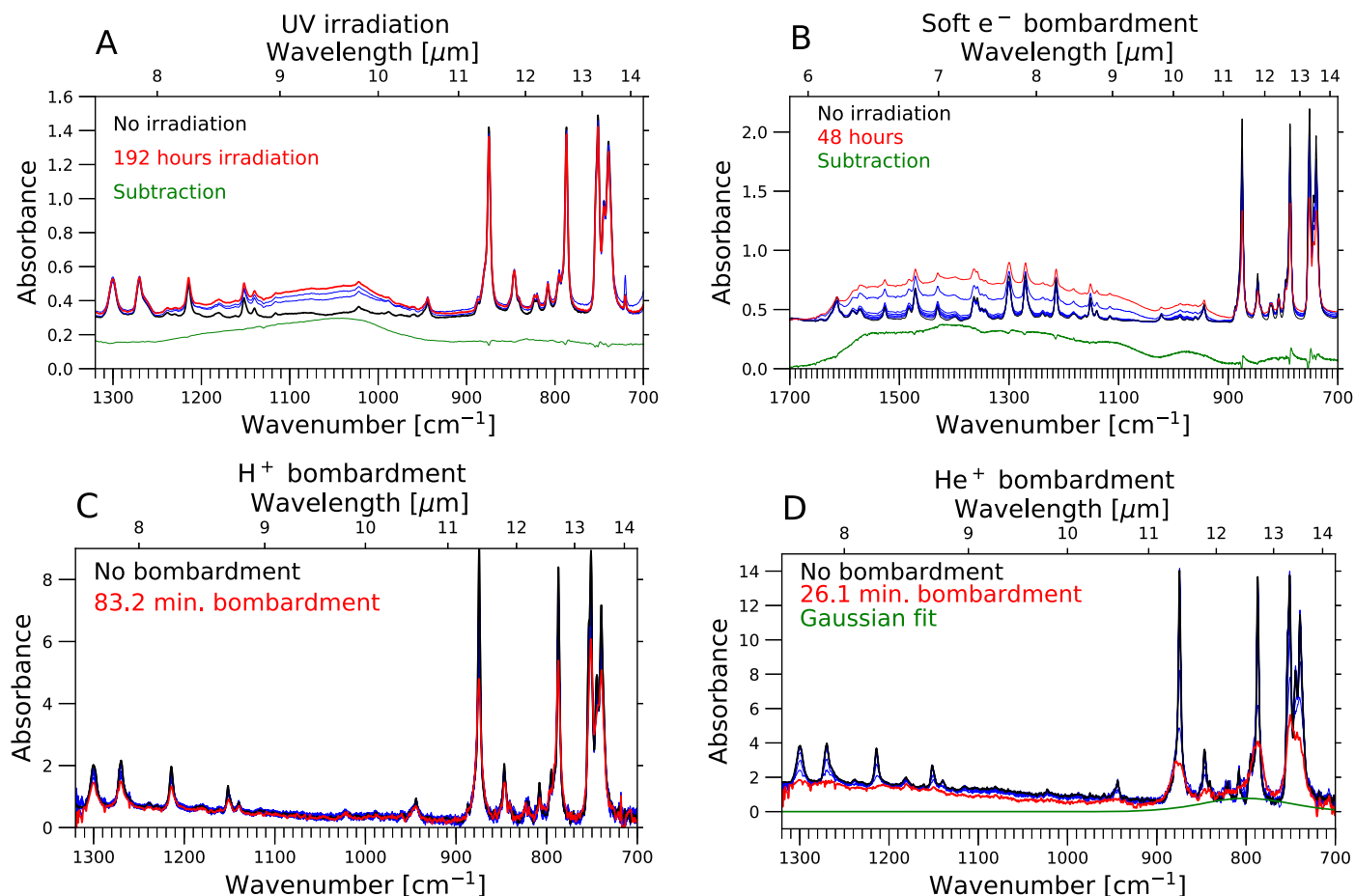


**Figure 7.** Spectra of IVA thin films processed by different energy sources: ultraviolet photons (A), soft electrons (B),  $H^+$  particles (C), and  $He^+$  particles (D). Black spectra in all plots correspond to the nonirradiated samples, red spectra to the last energetic processing, and blue spectra to irradiation times in between. The green trace is the difference spectrum of the final (red) and the initial (black) spectra. The experimental spectra have been normalized to  $1 \times 10^{15}$  molecules.

IVA bands remained at  $877.9$ ,  $842.1$ ,  $787.8$ , and  $750.6 \text{ cm}^{-1}$  ( $11.3$ ,  $11.8$ ,  $12.6$ , and  $13.3 \mu\text{m}$ ).

Using the Stopping and Range of Ions in Matter software (Ziegler et al. 2010), we have estimated, to within 10%, the penetration depth in IVA for  $1.5 \text{ MeV } H^+$  and  $He^+$  beams. The values are  $34.8$  and  $5.82 \mu\text{m}$ , respectively, lengths much longer than the thickness of IVA films ( $\approx 0.5 \mu\text{m}$ ). Thus, the  $H^+$  and  $He^+$  ions were going through the entire IVA thin films causing a bulk effect rather than a surface effect like UV photons and soft electrons. The  $H^+$  and  $He^+$  particles go through the whole film removing material and making tracks in the process.

### 3.2.4. $3.3 \mu\text{m}$ Feature

The observed  $3.3 \mu\text{m}$  feature had been associated with the C–H stretching region of PAHs. In the case of IVA in an argon matrix, intense bands were detected at  $3037.0$ ,  $3056.6$ ,  $3074.9$ , and  $3093.5 \text{ cm}^{-1}$ . Also, weaker peaks were identified at  $3010.5$ ,  $3018.0$ ,  $3101.0$ ,  $3106.5$ , and  $3118.0 \text{ cm}^{-1}$ ; see the red spectrum in Figure 9. Following Mattioda et al. (2017), we can assign the  $3037.0 \text{ cm}^{-1}$  band to the duo modes, the  $3056.6 \text{ cm}^{-1}$  band to the solo modes, the  $3074.9 \text{ cm}^{-1}$  band to the quartet modes, and the  $3074.9 \text{ cm}^{-1}$  to the bay regions. The bay regions in an IVA molecule are the space between the quartets and the duos, the space between two duos, the space between the duos and the solos, and the space between the solos and the quartets. The lower peaks can be assigned to

combo modes (combination modes of solos + duos + quartets) at  $3010.5$  and  $3018.0 \text{ cm}^{-1}$ , and the  $3101.0$ ,  $3106.5$ , and  $3118.0 \text{ cm}^{-1}$  bands to the bay regions.

There is an apparent difference between the IVA  $3.3 \mu\text{m}$  feature in an argon matrix and as a thin film (black spectrum in Figure 9). Combo modes in IVA thin film do not present any position shift ( $3010.5$  and  $3018.5 \text{ cm}^{-1}$ ) compared to IVA in an argon matrix; this is not the case for the other bands. Duo modes are centered at  $3031.3 \text{ cm}^{-1}$ , solo modes are centered at  $3046.4 \text{ cm}^{-1}$ , quartet modes are centered at  $3064.0 \text{ cm}^{-1}$ , and in the case of the bay modes, they are centered at  $3084.0$ ,  $3096.0$ , and  $3102.0 \text{ cm}^{-1}$ . Thus, these bands present redshifts of  $5.7$ ,  $10.2$ ,  $10.9$ , and  $9.5 \text{ cm}^{-1}$ , respectively, taking into account only the most intense band of the bay modes.

It is interesting to notice that the highest peak is for the quartets ( $3.25 \mu\text{m}$ ) for IVA in an argon matrix, while the highest peak is for the solos ( $3.28 \mu\text{m}$ ) for IVA as a thin film. Also, bands are more blended in the case of IVA thin film, as expected in the C–H stretching region.

Figure 10 shows the C–H stretching region of IVA as a thin film before (black spectrum), during (blue spectra), and after (red spectrum) irradiation by UV photons, soft electrons,  $H^+$ , and  $He^+$  particles. As previously stayed PAH molecules are resilient to irradiation, the C–H stretching region of IVA presented little changes after irradiation. For example, the decreasing of the C–H stretching region of IVA is minimal compared to the C–Hoop region during a soft electron

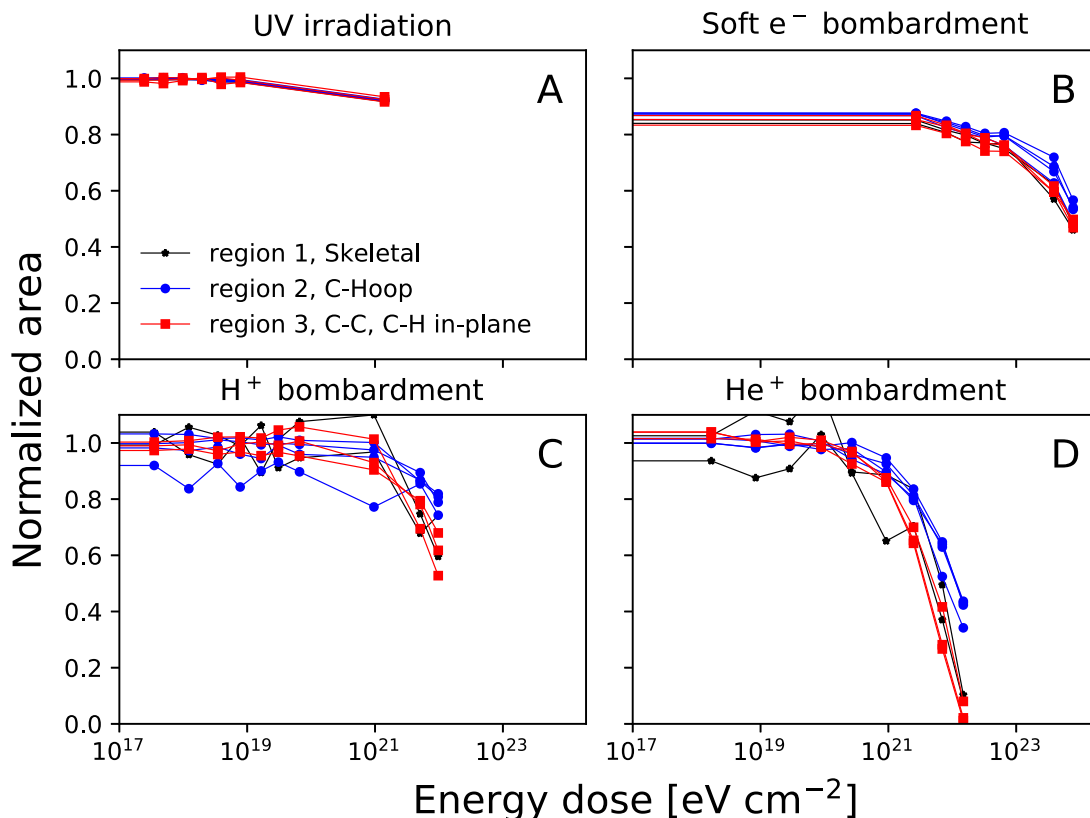


**Figure 8.** Normalized area as a function of energy dose for bands integrated over the three regions (skeletal modes, C-Hoop modes, C-C and C-H in-plane modes) of the IVA spectrum for different energy sources.

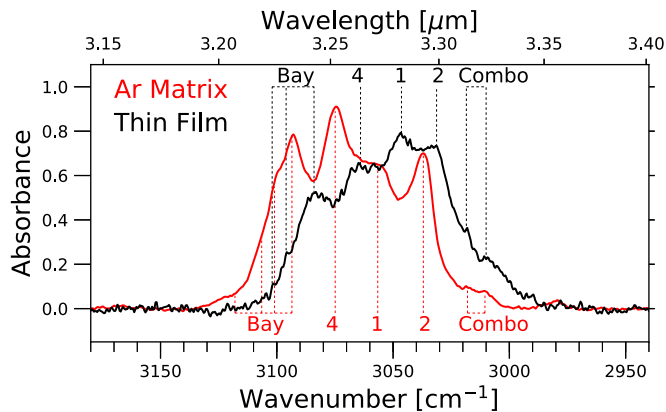


**Figure 9.** IVA deposition in Ar matrix (red) compared with IVA deposited as a thin film (black). Experimental spectra have been normalized to  $1 \times 10^{15}$  molecules.

bombardment; see Table 6. Nevertheless, the  $\text{He}^+$  bombardment of IVA as a thin film produced an increment in the area for the C-H stretching region. This result may be related to the broadening of the C-Hoop bands reported previously.

### 3.2.5. Comparison among Energy Sources

Figure 11 shows the effect of different radiation sources on a PAH thin-film structure. Broad features or plateaus grow with radiation exposure after the sample was processed with UV photons, electrons, and  $\text{He}^+$  particles. These features are centered at 9.6, 7.7, and 12.5  $\mu\text{m}$ , respectively. Although

broad, these features can be distinguished between one another and could be used to separate the effect of different energy sources on PAHs. These broad features could be the manifestation of refractory material building up on top of the IVA, cross-linking of PAH layers, or a process of PAH hydrogenation.

UV photons and soft electrons, unlike the  $\text{H}^+$  and  $\text{He}^+$  particles, do not have the energy necessary to penetrate the IVA thin film completely. After conducting blank experiments (see Figure 13 in the Appendix), some broad features were detected. They have been taken into account for the interpretation of the results; see the Appendix.

Egerton et al. (2010) reported the energy needed for incident electrons to produce sputtering for different elements. In the case of carbon, they gave a minimum energy of 68 keV but also commented that a value of 86 keV had been reported for a carbon nanotube. This energy is above the electron energy used in our experiments; hence, we do not expect soft energy electrons to produce any sputtering of the IVA.

In the ion interaction with PAHs, several processes can play a crucial role, e.g., charge exchange, electronic stopping, and fragmentation; see Postma et al. (2010). PAHs can be destroyed by inertial or thermal carbon sputtering in high-velocity shocks; see Micelotta et al. (2010). In the case of  $\text{He}^+$  bombardment, sputtering may be an essential process to consider. It could degrade IVA at a high rate with one of the effects being the broadening of the IR modes. Since mass spectrometry was not performed during the experiments, it is difficult to quantify the effect of this process, and we cannot rule it out.

Seperuelo Duarte et al. (2009, 2010) reported that for a CO ice, the sputtering yield is constant during the irradiation, while

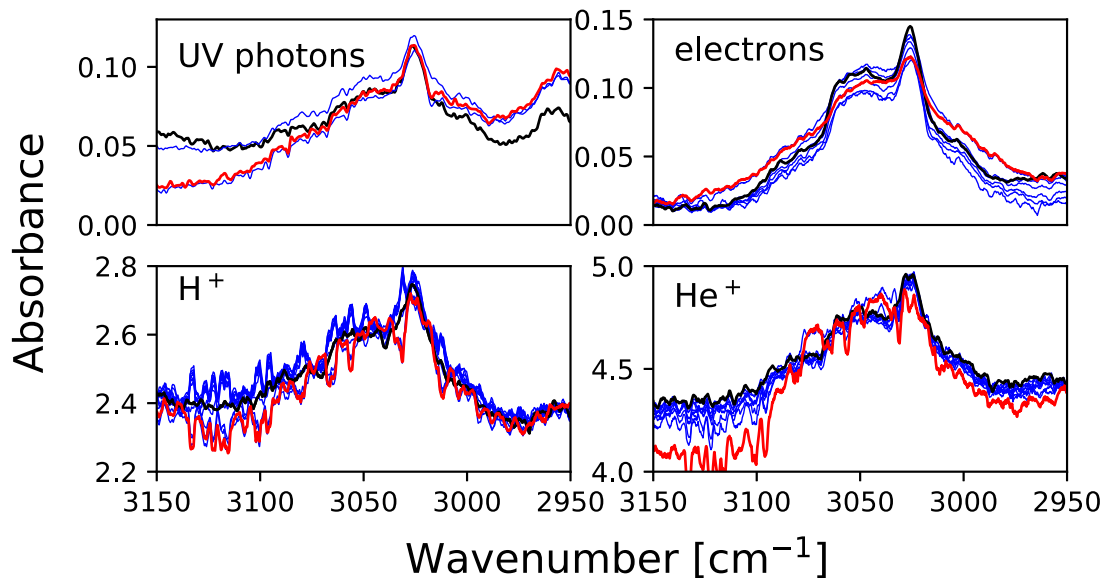


**Figure 10.** Aromatic C–H stretching region of IVA before and after irradiation with different energy sources.

**Table 6**  
The Decrease Rates of Neutral IVA by Incident UV Photons, Ion, and Electron Particles in Matrix Isolation and Thin Film

Radiation source	Matrix Isolation		Thin Film			
	UV (10.2 eV)	UV (10.2 eV)	e <sup>-</sup> (1.5 keV)	H <sup>+</sup> (1.5 MeV)	He <sup>+</sup> (1.5 MeV)	
Sample thickness	Argon 170 μm	Water 1.5 μm	0.45 μm			
Decrease rate (s <sup>-1</sup> )	0.02	0.03	0.02	0.07	0.09	0.16
C–H stretching						
Decrease rate (s <sup>-1</sup> )	1.4 × 10 <sup>-4</sup>	2.5 × 10 <sup>-7</sup>	1.3 × 10 <sup>-6</sup>	2.5 × 10 <sup>-5</sup>	<sup>a</sup> 3.4 × 10 <sup>-4</sup>	

**Note.** The normalized IVA column density in each experiment was used for calculations.

<sup>a</sup> In the case of He<sup>+</sup> bombardment, the rate reported in the C–H stretching is a growth rate.

radiolysis (a bulk process) decreases with fluence once the CO sample goes thinner. The sputtering yield in CO ice depends on the square of the electronic stopping power. In contrast, radiolysis cross sections raise to the power of  $\frac{3}{2}$  (Andrade et al. 2013). This means that, for swift heavy ions, with considerable stopping power, sputtering dominates the sample modification. In the case of H<sup>+</sup> and He<sup>+</sup> bombardment with relatively low energy, the role of sputtering is less relevant. Moreover, for organic material, refractory material builds up on top of the sample reducing the IVA sputtering rate progressively.

The decrease rate (in s<sup>-1</sup>) for the different energy sources was calculated using the normalized decrease in the neutral IVA IR modes (normalized column density) and the irradiation time of the sources, and are provided in Table 6; for completeness, we included the decrease rates for the matrix-isolation experiments. In this instance, we refer to decrease as the loss of intensity of the IVA neutral IR modes. This loss could be by the ionization of neutral IVA, the destruction of the IVA molecule, or the creation of a product by radical interaction. In the case of He<sup>+</sup> bombardment, the rate reported in the C–H stretching is a growth rate since the integration of the C–H stretching region did not decrease but increased with bombardment time.

#### 4. Discussion and Implications for Astronomy

It has been suggested that PAH molecules could agglomerate and produce clusters or small grains, which then freeze out onto dust grain particles or act like nano-size dust grains allowing them to interact with other molecules within ice mantles (Allamandola et al. 1989; Rapacioli et al. 2006; Tielens 2008; Steglich et al. 2010). Being that PAHs are such ubiquitous molecules in the universe, it is logical to think that H, O, and OH enriched PAH molecules exist in the interstellar medium, where water dominates the infrared spectrum of ice mantles (Bernstein et al. 1999, 2002; Sandford et al. 2000; Bouwman et al. 2011; de Barros et al. 2017; this work).

The estimated percentage abundance for H<sub>2</sub>O<sub>2</sub> on Europa (a potential reservoir for organic molecules) is 0.07% to 0.28%, according to Carlson et al. (1999). When Zheng et al. (2006) bombarded water ice with 5 keV electrons, they were able to produce 0.02%, 0.5%, 0.7%, and 0.8% of H<sub>2</sub>O<sub>2</sub> relative to water depending on the electron flux. Gomis et al. (2004) showed similar results irradiating water ice with ions reporting production of H<sub>2</sub>O<sub>2</sub> relative to water of 1.2% for H<sup>+</sup>, 2.4% for He<sup>+</sup>, and 6% for Ar<sup>++</sup> bombardment. In the case of UV, Gerakines et al. (1995) obtained a H<sub>2</sub>O<sub>2</sub> production of 2.1% relative to water. Our H<sub>2</sub>O<sub>2</sub> production (0.2% with respect to



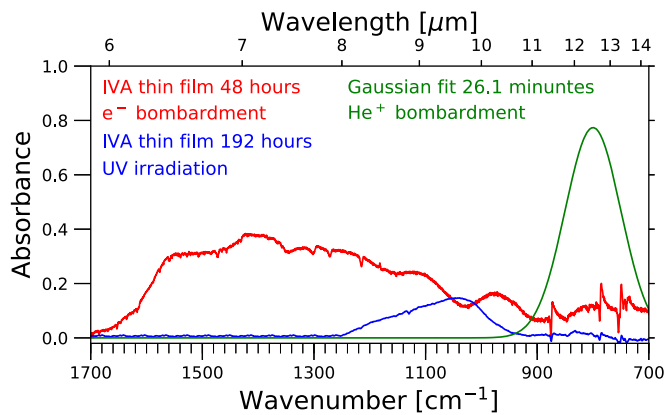


**Figure 11.** Comparison of the difference spectra for the various energy sources. Electron bombardment (red), UV irradiation (blue), and Gaussian fit for the  $\text{He}^+$  bombardment (green). Spectra have been normalized to  $1 \times 10^{15}$  molecules.

water) is 10 times lower than Gerakines et al. (1995), possibly because the OH radicals reacted with IVA to form IVA alcohol photoproducts. It is interesting to notice that our  $\text{H}_2\text{O}_2$  production is in the range of what was found in Europa.

The plateaus produced by UV photons and soft electrons are a consequence of a surface effect taking place on the IVA thin film. Irradiation with UV photons and soft electrons produces radicals that can degenerate the IVA via hydrogenation. Annealing was not considered to be the process responsible for these broad features since it broadens existing vibrational bands rather than creating new spectral features.

IVA bands disappeared entirely in regions 1 and 3 while others remained with different band profiles in regions 2 and 4 (C-Hoop and C-H stretching) for  $\text{He}^+$  bombardment. The broad feature centered at  $12.5 \mu\text{m}$  is more likely to be annealing of the C-Hoop modes since the C-H stretching modes presented a similar broadening effect. This result suggests that low-energy irradiation of PAH has a surface effect; meanwhile, high-energy irradiation has a likely bulk effect.

Calcagno et al. (1994) studied the cross-linking in mono-disperse polystyrene induced by energetic ion bombardment. They used  $\text{H}^+$ ,  $\text{He}^+$ , and  $\text{C}^+$  with a wide range of energies (10 keV–9.0 MeV). The chemical yield (the efficiency of an ion beam for producing cross-linking) was measured for each ion, and they found that it is higher for lower energies and that it decreases with higher ion energies. They explained that the spatial distribution of microscopic energy deposition is more localized for low-velocity ions. This result could explain the different outcomes for IVA irradiation reported here, where electrons with a 1.5 keV energy produced higher chemical reactions than  $\text{H}^+$  and  $\text{He}^+$  particles.

Figure 7 shows that IVA destruction does not occur at the same energy dose for different energy sources. This discrepancy is because the destruction cross-section is not directly proportional to the energy dose (or to the stopping power), it depends on the power  $\frac{3}{2}$  as previously stated; see Pereira et al. (2019). 1.5 MeV  $\text{H}^+$  and 1.5 MeV  $\text{He}^+$  have different stopping powers. This difference cannot be compensated for by increasing or decreasing the fluence to the same ratio getting the same dose. Molecular destruction is not directly proportional to the energy dose in this sense.

The identified broad features are well separated depending on the energy source, indicating that each feature is dependent

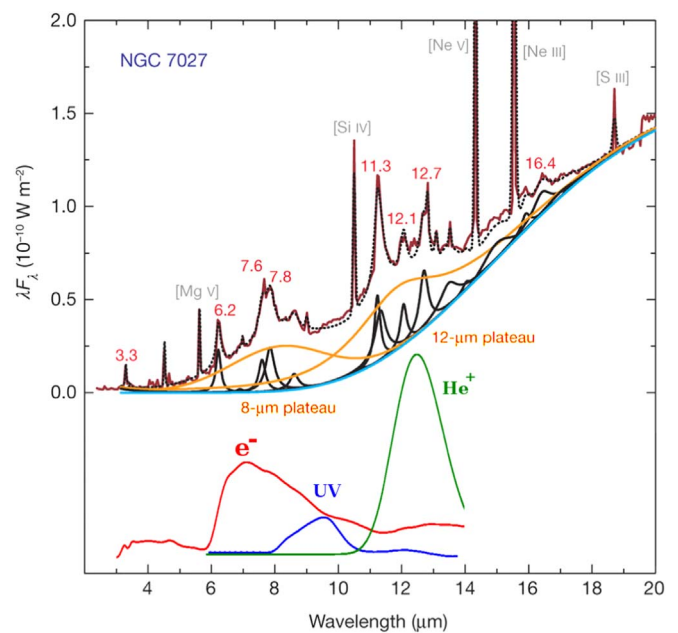


**Figure 12.** Figure from Kwok & Zhang (2011). It shows the NGC 7027 infrared spectrum in the 4 to 16  $\mu\text{m}$  region. Superposed, and below, are our data for the IVA thin film after 26.1 minutes of  $\text{He}^+$  bombardment (green), the subtraction spectrum after 48 hr of electron bombardment (red), and the subtraction spectrum after 192 hr of UV irradiation (blue). The original figure has been cut for clarity. Experimental spectra have been normalized to  $1 \times 10^{15}$  molecules.

on a particular irradiation processing of the thin film. Characterizing the formation of these features is crucial since they could be used as a diagnostic tool for astronomers.

Peeters et al. (2017) assigned the 10 to 15  $\mu\text{m}$  plateau to a dust continuum emission, which means that plateaus are separated from the PAH emission features. According to our experiments, plateau-like features can be produced after PAHs are exposed to an energy source. Hence, plateaus could be the manifestation of energetically processed PAHs.

Plateaus centered at 8 and 12  $\mu\text{m}$  are easily spotted in the infrared spectrum of the protoplanetary nebulae NGC 7027. These plateaus are similar to the broad features reported here at 9.6, 7.7, and 12.5  $\mu\text{m}$ ; see Figure 12. This figure is a composition of Figure 1(a) in Kwok & Zhang (2011) and the smoothed spectra of the broad features produced in our experiments. The broad features produced in the laboratory can be associated with the observed plateaus in Figure 12. PAHs are great carrier candidates to the observed mid-infrared bands since they can survive the harsh environment of the protoplanetary nebulae NGC 7027.

PAHs can be degraded by fragmentation via H-atom or  $\text{C}_2\text{H}_2$  loss (Micelotta et al. 2010). The destruction process is dominated by ions like  $\text{He}^+$  at temperatures below  $3 \times 10^4$  K and by electrons above this value. We have shown with our experiments that UV photons and soft electrons do not destroy PAHs efficiently, but  $\text{He}^+$  particles do. Nevertheless, UV photons and soft electrons produce new broad features while  $\text{He}^+$  particles generated annealing in the C-Hoop and C-H stretching regions.

## 5. Conclusions

This work described the mid-IR absorption spectroscopy of IVA in an argon matrix and a water matrix and as a thin film.

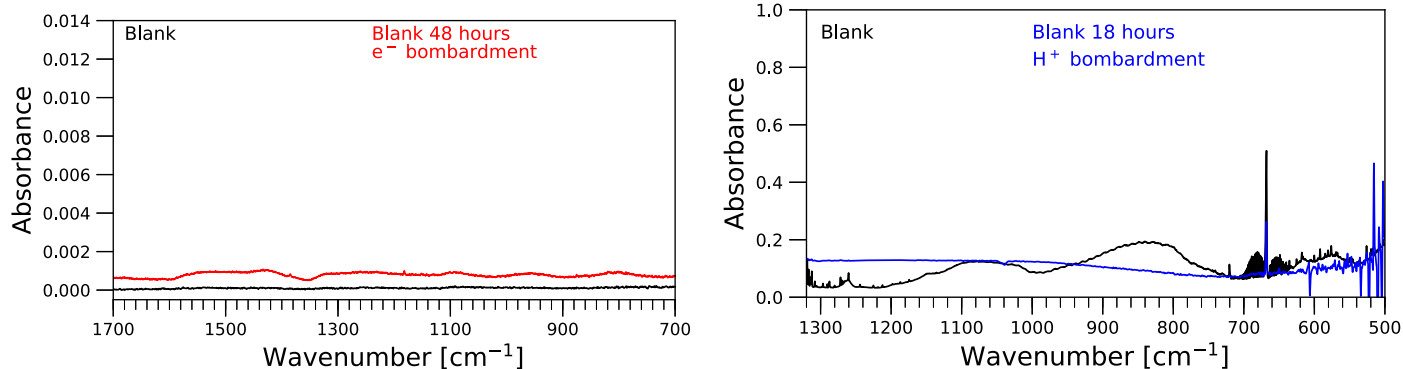


**Figure 13.** Blank window exposure. Left: CsI window blank, no irradiation (black) and after 48 hr of electron irradiation (red). Right: KBr window blank, no irradiation (black) and after 18 hr of H<sup>+</sup> irradiation (blue).

Both anions and cations were produced upon UV irradiation in an argon matrix. The water-matrix experiments did not produce any IVA<sup>-</sup>, but IVA<sup>+</sup> and protonated and oxygenated photoproducts were identified as the result of the UV irradiation. UV photons are more likely to produce IVHOH<sup>+</sup> and IVH<sup>+</sup>, but their neutral counterparts IVHOH and IVH cannot be ruled out. IVO and IVO<sup>+</sup> were not produced based on their comparison with theoretical data. It seems the presence of aromatics in water ice reduces the formation of H<sub>2</sub>O<sub>2</sub> by one order of magnitude, bringing the H<sub>2</sub>O<sub>2</sub> values in line with those estimated for Europa.

Thin-film experiments (mimicking a PAH cluster or a nano-size PAH particle) showed that for long periods of UV irradiation a broad feature (8.0 to 10.5 μm) centered at 9.6 μm appears while the overall mid-IR bands did not significantly decrease. For soft electron bombardment, PAH bands decreased faster with a broad feature (9.7 to 11.1 μm) centered at 7.7 μm appearing upon bombardment.

H<sup>+</sup> bombardment of IVA thin films produced a decreasing in mid-IR bands at a faster rate than UV photons and soft electron bombardment, but no broad feature was detected. He<sup>+</sup> bombardment destroyed PAH molecules the fastest with only the C-Hoop and C-H stretching bands remaining in the spectrum. A broad feature (11.0 to 14.5 μm) centered at 12.5 μm was observed as a result of the annealing of the bands in the C-Hoop region. This annealing was also detected for the C-H stretching region.

This work was supported by the National Aeronautics and Space Administration and by the Brazilian CAPES Agency under the scholarship BEX 5383/15-3 grant. This material is based upon work supported by the National Aeronautics and Space Administration through the NASA Astrobiology Institute under Cooperative Agreement Notice NNX13ZDA017C issued through the Science Mission Directorate. A.R. gratefully acknowledges support from NASA's Exobiology Program (NNX13AJ08G).




### Appendix Blank Experiments

Samples were irradiated using high-energy particles (electrons, H<sup>+</sup>, and He<sup>+</sup>). These energy sources present a high penetration depth that could cause some damage (e.g., development of color centers) to the windows used for the deposition of IVA. The IR could detect this damage as features, and hence they could interfere with the results. Avoiding false

detections is essential; this is why the windows used for deposition were irradiated, using the sources mentioned above, checking for features after exposure. Figure 13 shows the two windows used for sample deposition (CsI on the left and KBr on the right) before and after irradiation. In the case of electron irradiation, the spectrum after irradiation presents a small waved pattern compared to the nonirradiated one. However, comparing the spectrum after irradiation in Figure 13 to the spectrum of IVA after electron irradiation in Figure 11, it is clear that electron irradiation does not produce any significant feature on a blank window. In the case of H<sup>+</sup> irradiation, Figure 13 shows that there are features comparable to the UV irradiation feature in Figure 11.

Nevertheless, the spectrum showing these features is the spectrum before irradiation, and it is easy to notice that the spectrum after irradiation does not present any feature. H<sup>+</sup> irradiation of a blank window may not produce any feature. He<sup>+</sup> irradiation of a blank window was not possible, but a similar behavior like H<sup>+</sup> irradiation is expected. Nonetheless, the broad feature reported as a He<sup>+</sup> irradiation effect is not a window feature but a broadening of the IVA IR bands caused by the damage taken from the high-energy exposure. UV irradiation does not have enough energy to produce any alteration to the deposition windows.

### ORCID iDs

G. A. Cruz-Diaz  <https://orcid.org/0000-0003-2270-6103>  
 A. Ricca  <https://orcid.org/0000-0002-3141-0630>  
 A. L. F. de Barros  <https://orcid.org/0000-0001-7023-8282>

### References

- Alata, I., Cruz-Diaz, G. A., Muñoz Caro, G. M., & Dartois, E. 2014, *A&A*, **569**, A119  
 Allamandola, L. J., Tielens, A. G. G. M., & Barker, J. R. 1989, *ApJS*, **71**, 733  
 Andrade, D. P. P., de Barros, A. L. F., Pilling, S., et al. 2013, *MNRAS*, **430**, 787  
 Behlen, F. M., McDonald, D. B., Sethuraman, V., & Rice, S. A. 1981, *JChPh*, **75**, 5685  
 Bernstein, M. P., Dworkin, J. P., Sandford, S. A., & Allamandola, L. J. 2001, *M&PS*, **36**, 351  
 Bernstein, M. P., Dworkin, J. P., Sandford, S. A., & Allamandola, L. J. 2002, *AdSpR*, **30**, 1501  
 Bernstein, M. P., Sandford, S. A., Allamandola, L. J., et al. 1999, *Sci*, **283**, 1135  
 Blasberger, A., Behar, E., Perets, H. B., Brosch, N., & Tielens, A. G. G. M. 2017, *ApJ*, **836**, 173  
 Bouwman, J., Mattioda, A. L., Linnartz, H., & Allamandola, L. J. 2011, *A&A*, **525**, A93

- Bramall, N. E., Quinn, R. C., Mattioda, A. L., et al. 2012, *P&SS*, **60**, 121
- Calcagno, L., Percolla, R., & Foti, G. 1994, *NIMPB*, **95**, 59
- Cané, E., Miani, A., Palmieri, P., Tarroni, R., & Trombetti, A. 1997, *JChPh*, **106**, 9004
- Carlson, R. W., Anderson, M. S., Johnson, R. E., et al. 1999, *Sci*, **283**, 2062
- Chen, Y.-J., Chuang, K.-J., Muñoz Caro, G. M., et al. 2014, *ApJ*, **781**, 15
- Cook, A., Mattioda, A. L., Quinn, R. C., et al. 2014, *ApJS*, **210**, 15
- Cook, A. M., Ricca, A., Mattioda, A. L., et al. 2015, *ApJ*, **799**, A93
- Cruz-Diaz, G. A., Muñoz Caro, G. M., Chen, Y.-J., & Yih, T.-S. 2014, *A&A*, **562**, A119
- d'Hendecourt, L. B., & Allamandola, L. J. 1986, *A&AS*, **64**, 453
- de Barros, A. L. F., Mattioda, A. L., Ricca, A., Cruz-Diaz, G. A., & Allamandola, L. J. 2017, *ApJ*, **848**, 112
- Egerton, R. F., McLeod, R., Wang, F., & Malac, M. 2010, *Ultmi*, **110**, 991
- Ehrenfreund, P., Ricco, A. J., Squires, D., et al. 2014, *AcAau*, **93**, 501
- Fitzpatrick, E. L., & Massa, D. 2007, *ApJ*, **663**, 320
- Gerakines, P. A., Schutte, W. A., Greenberg, J. M., & van Dishoeck, E. F. 1995, *A&A*, **296**, 810
- Gomis, O., Leto, G., & Strazzulla, G. 2004, *A&A*, **420**, 405
- Halasinski, T. M., Salama, F., & Allamandola, L. J. 2005, *ApJ*, **628**, 555
- Hudgins, A. M., Sandford, S. A., & Allamandola, L. J. 1994, *JPhCh*, **98**, 4243
- Kwok, S., & Zhang, Y. 2011, *Natur*, **479**, 80
- Kyriakou, I., Emfietzoglou, D., Nojeh, A., & Moscovitch, M. 2013, *JAP*, **113**, 084303
- Mattioda, A. L., Bauschlicher, C. W., Jr, Ricca, A., et al. 2017, *AcSpA*, **181**, 286
- Mattioda, A. L., Cook, A., & Ehrenfreund, P. 2012, *AsBio*, **12**, 841
- Mattioda, A. L., Hudgins, D. M., Bauschlicher, C. W., Jr, & Allamandola, L. J. 2005, *AdSpR*, **36**, 156
- Mattioda, A. L., Hudgins, D. M., Bauschlicher, C. W., Jr, Rosi, M., & Allamandola, L. J. 2003, *JPCA*, **107**, 1486
- Micelotta, E. R., Jones, A. P., & Tielens, A. G. G. M. 2010, *A&A*, **510**, A37
- Micelotta, E. R., Jones, A. P., & Tielens, A. G. G. M. 2011, *A&A*, **526**, A52
- Moore, M. H., & Hudson, R. L. 2000, *Icar*, **145**, 282
- Peeters, E., Bauschlicher, C. W., Jr, Allamandola, L. J., et al. 2017, *ApJ*, **836**, 198
- Pereira, R. C., de Barros, A. L. F., Fulvio, D., et al. 2019, *NIMPB*, in press
- Pilling, S., Mendes, L. A. V., Bordalo, V., et al. 2013, *AsBio*, **13**, 79
- Pirali, O., Vervloet, M., Mulas, G., Mallocci, G., & Joblin, C. 2009, *PCCP*, **11**, 3443
- Postma, J., Bari, S., Hoekstra, R., Tielens, A. G. G. M., & Schlathölter, T. 2010, *ApJ*, **708**, 1
- Rapacioli, M., Calvo, F., Joblin, C., et al. 2006, *A&A*, **460**, 519
- Rapacioli, M., Calvo, F., Spiegelman, F., Joblin, C., & Wales, D. J. 2005, *JPCA*, **109**, 2487
- Sandford, S. A., Bernstein, M. P., Allamandola, L. J., Gillette, J. S., & Zare, R. N. 2000, *ApJ*, **538**, 691
- Savage, B. D., Massa, D., Meade, M., & Wesselius, P. R. 1985, *ApJ*, **59**, 397
- Seperuelo Duarte, E., Boduch, P., Rothard, H., et al. 2009, *A&A*, **502**, 599
- Seperuelo Duarte, E., Domaracka, A., Boduch, P., et al. 2010, *A&A*, **512**, A71
- Sloan, G. C., Lagadec, E., & Zijlstra, A. A. 2014, *ApJ*, **791**, 28
- Stecher, T. P. 1965, *ApJ*, **142**, 1683
- Steglich, M., Carpentier, Y., Jäger, C., et al. 2012, *A&A*, **540**, A110
- Steglich, M., Jäger, C., Rouille, G., et al. 2010, *ApJL*, **712**, L16
- Tielens, A. G. G. M. 2008, *ARA&A*, **46**, 289
- Truica-Marasescu, F.-E., & Wertheimer, M. R. 2005, *MmCP*, **206**, 744
- Valencic, L. A., Clayton, G. C., & Gordon, K. D. 2004, *ApJ*, **616**, 912
- Zheng, W., Jewitt, D., & Kaiser, R. I. 2006, *ApJ*, **639**, 534
- Ziegler, J. F., Ziegler, M. D., & Biersack, J. P. 2010, *NIMPB*, **268**, 1818